Inorganic Chemistry
Article

Inorg. Chem. **2010**, *49*, 5393–5406 **5393**
DOI: 10.1021/ic9023053

Bisamidate and Mixed Amine/Amidate NiN_2S_2 Complexes as Models for Nickel-Containing Acetyl Coenzyme A Synthase and Superoxide Dismutase: An Experimental and Computational Study

Vaidyanathan Mathruboothan,[†] Jason Thomas,[†] Richard Staples,[‡] John McCraken,[‡] Jason Shearer,[*,§] and Eric L. Hegg[*,†]

[†]*Department of Biochemistry & Molecular Biology, and* [‡]*Department of Chemistry, Michigan State University, East Lansing, Michigan 48824, and* [§]*Department of Chemistry, University of Nevada, Reno, Nevada 89557*

Received November 23, 2009

The distal nickel site of acetyl-CoA synthase (Ni_d-ACS) and reduced nickel superoxide dismutase (Ni-SOD) display similar square-planar $Ni^{II}N_2S_2$ coordination environments. One difference between these two sites, however, is that the nickel ion in Ni-SOD contains a mixed amine/amidate coordination motif while the Ni_d site in Ni-ACS contains a bisamidate coordination motif. To provide insight into the consequences of the different coordination environments on the properties of the Ni ions, we systematically examined two square-planar $Ni^{II}N_2S_2$ complexes, one with bisthiolate-bisamidate ligation $(Et_4N)_2(Ni(L1))\cdot 2H_2O$ (**2**) [H_4L1 = *N*-(2-mercaptoacetyl)-*N*′-(2-mercaptoethyl)glycinamide] and another with bisthiolate-amine/amidate ligation K(Ni(HL2)) (**3**) [H_4L2 = *N*-(2′′-mercaptoethyl)-2-((2′-mercaptoethyl)amino)acetamide]. Although these two complexes differ only by a single amine versus amidate ligand, their chemical properties are quite different. The stronger in-plane ligand field in the bisamidate complex $(Ni^{II}(L1))^{2-}$ (**2**) results in an increase in the energies of the d → d transitions and a considerably more negative oxidation potential. Furthermore, while the bisamidate complex $(Ni^{II}(L1))^{2-}$ (**2**) readily forms a trinuclear species $(Et_4N)_2(\{Ni(L1)\}_2\text{-}Ni)\cdot H_2O$ (**1**) and reacts rapidly with O_2, presumably via sulfoxidation, the mixed amine/amidate complex $(Ni^{II}(HL2))^{-}$ (**3**) remains monomeric and is stable for days in air. Interestingly, the Ni^{III} species of the bisamidate complex formed by chemical oxidation with I_2 can be detected by electron paramagnetic resonance (EPR) spectroscopy while the mixed amine/amidate complex immediately decomposes upon oxidation. To explain these experimentally observed properties, we performed S K-edge X-ray absorption spectroscopy and low-temperature (77 K) electronic absorption measurements as well as both hybrid density functional theory (hybrid-DFT) and spectroscopy oriented configuration interaction (SORCI) calculations. These studies demonstrate that the highest occupied molecular orbital (HOMO) of the bisamidate complex $(Ni^{II}(L1))^{2-}$ (**2**) has more Ni character and is significantly destabilized relative to the mixed amine/amidate complex $(Ni^{II}(HL2))^{-}$ (**3**) by ∼6.2 kcal mol^{-1}. The consequence of this destabilization is manifested in the nucleophilic activation of the doubly filled HOMO, which makes $(Ni^{II}(L1))^{2-}$ (**2**) significantly more reactive toward electrophiles such as O_2.

Introduction

Nickel is an essential trace element for bacteria, plants, animals, and humans. To date, several nickel-containing enzymes are known and have been structurally characterized.[1−4] Nickel enzymes can be divided into two groups: hydrolases and redox enzymes. In the hydrolase nickel enzymes, the nickel ion is found to exist only in the Ni^{II} state, and the Ni-center acts as a Lewis acid. The five known Ni redox enzymes are [NiFe]-hydrogenases, CO dehydrogenase (CODH), acetyl-CoA synthase (ACS), methyl-coenzyme reductase (MCR), and nickel-dependent superoxide dismutase (Ni-SOD).[1−4] A common feature in redox active nickel enzymes is the presence of thiolate coordination, which helps the nickel centers access different oxidation states in their catalytic cycles.[4] In spite of several physical and biochemical

*To whom correspondence should be addressed. E-mail: erichegg@msu.edu (E.L.H.), shearer@chem.unr.edu (J.S.).

(1) (a) *Nickel and its surprising Impact in Nature*; Sigel, A., Sigel, H., Sigel, R. K. O., Eds.; John Wiley & Sons: Chichester, U.K., 2007; Metal ions in Life Sciences, Vol. *2*. (b) *The Bioinorganic Chemistry of Nickel*; Lancaster, J. R., Jr., Ed.; VCH: New York, 1988.

(2) (a) Ragsdale, S. W. Nickel Enzymes & Cofactors. In *Encyclopedia of Inorganic Chemistry* [*online*]; King, R. B., Ed.; John Wiley & Sons: Chichester, U.K., 2005; pp 1−16; http://mrw.interscience.wiley.com/emrw/9780470862100/eic/article/ia149/current/pdf (accessed March 2, 2010). (b) Ragsdale, S. W. *J. Inorg. Biochem.* **2007**, *101*, 1657–1666. (c) Ragsdale, S. W. *J. Biol. Chem.* **2009**, *284*, 18571–18575.

(3) Halcrow, M. A.; Christou, G. *Chem. Rev.* **1994**, *94*, 2421–2481.

(4) (a) Maroney, M. J.; Davidson, G.; Allan, C. B.; Figlar, J. *Struct. Bonding* **1998**, *92*, 1–65. (b) Maroney, M. J. *Curr. Opin. Chem. Biol.* **1999**, *3*, 188–199.

Published on Web 05/27/2010

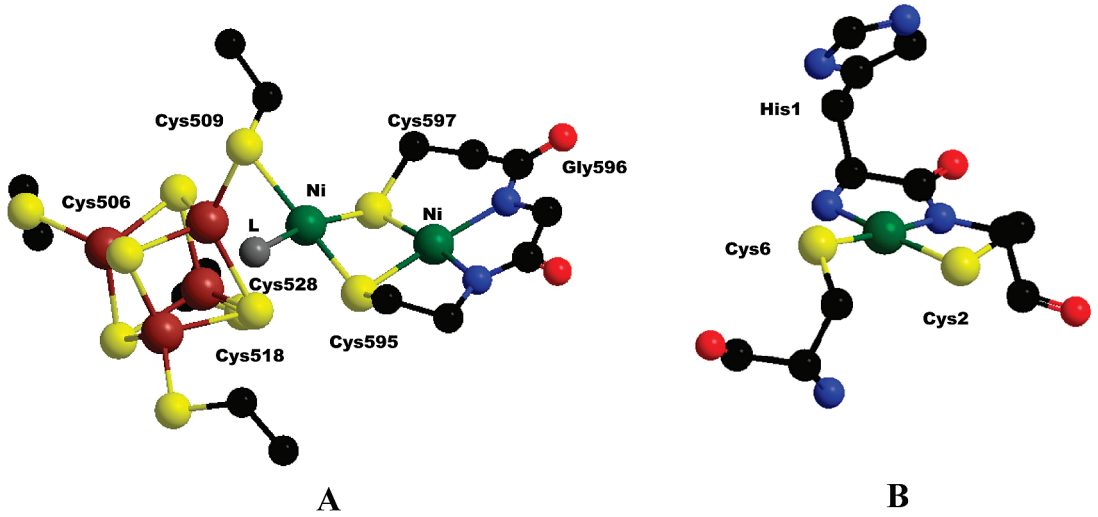

Figure 1. Active site structure of (A) Ni-ACS and (B) reduced Ni-SOD. (Structures prepared from the coordinates obtained from Protein Data Bank files 1OAO and 1T6U respectively for Ni-ACS and Ni-SOD, refs 9 and 26b, respectively.)

studies on these enzymes,[1−5] it is still not fully understood how the different ligand environments facilitate the catalysis of such a wide range of reactions. The main goals of this study are to elucidate how the NiN_2S_2 coordination environment found in Ni-SOD and the distal Ni site of CODH/ACS contributes to the different properties of these two nickel ions and to quantify these effects.

The metalloenzyme carbon monoxide dehydrogenase/acetyl coenzyme A synthase (CODH/ACS) is an unusual bifunctional enzyme present in a number of acetogenic, methanogenic, and sulfate-reducing bacteria.[5−7] In the first step, CO_2 is reduced to CO at the C-cluster (CODH activity). The subsequent formation of acetyl-CoA from CO, a methyl group, and coenzyme A is catalyzed by the A-cluster (ACS activity). Crystal structures of the A-cluster of ACS/CODH[8,9] as well as the monomeric form of ACS[10] have been reported. The active site contains a unique dinuclear nickel center linked to a $[Fe_4S_4]$ cluster (Figure 1A).[8−12] The proximal nickel (Ni_p) is coordinated to three cysteine thiolates and an unidentified exogenous ligand while the distal square-planar nickel (Ni_d) is ligated in an unusual Cys-Gly-Cys motif consisting of two deprotonated amides and two cysteine thiolates.[8−10] Acetyl-CoA is presumably synthesized at Ni_p; it is generally believed that Ni_d is not involved in redox chemistry and that the nickel ion remains in the Ni^{II} state throughout the catalytic cycle, although this remains to be definitively verified.[2,6b,13]

Despite the availability of three high-resolution crystal structures for ACS and nearly two decades of thorough spectroscopic and biochemical studies, many questions remain concerning the role of the endogenous ligands in tuning the properties of the Ni ions.[13] To address these questions, we[14] and others[15−21] synthesized small metal complexes that serve as well-defined mimics of the active site. Ironically, Holm[22] and Krüger[22,23] developed some of the earliest models of the Ni_d(Cys-Gly-Cys) site when preparing models for the active site of [NiFe]-hydrogenases well before the structure of ACS was known. Since the elucidation of the ACS crystal structure, considerable effort has been directed toward modeling the dinuclear nickel active site (Ni_p-Ni_d site), and several laboratories have reported on various aspects of the dinuclear Ni−Ni site.[14−21] Unfortunately, attempts to synthesize discrete dinuclear ACS models often

(5) Ragsdale, S. W.; Kumar, M. *Chem. Rev.* **1996**, *96*, 2515–2539.
(6) (a) Lindahl, P. A. *Biochemistry* **2002**, *41*, 2097–2105. (b) Lindahl, P. A.; Graham, D. E. In *Nickel and Its Surprising Impact in Nature*; Sigel, A., Sigel, H., Sigel, R. K. O., Eds.; John Wiley & Sons: Chichester, U.K., 2007; Metal ions in Life Sciences, Vol. *2*, Chapter 9, pp 357−411.
(7) (a) Ragsdale, S. W. *Crit. Rev. Biochem. Mol. Biol.* **2004**, *39*, 165–195. (b) Ragsdale, S. W. *Biofactors* **1997**, *6*, 3–9.
(8) Doukov, T. I.; Iverson, T. M.; Servalli, J.; Ragsdale, S. W.; Drennan, C. L. *Science* **2002**, *298*, 567–572.
(9) Darnault, C.; Volbeda, A.; Kim, E. J.; Legrand, P.; Vernede, X.; Lindahl, P. A.; Fontecilla-Camps, J. C. *Nat. Struct. Biol.* **2003**, *10*, 271–279.
(10) Svetlitchnyi, V.; Dobbek, H.; Meyer-Klaucke, W.; Meins, T.; Thiele, B.; Römer, P.; Huber, R.; Meyer, O. *Proc. Natl. Acad. Sci. U.S.A.* **2004**, *101*, 446–451.
(11) (a) Shin, W.; Anderson, M. E.; Lindahl, P. A. *J. Am. Chem. Soc.* **1993**, *115*, 5522–5526. (b) Bramlett, M. R.; Tan, X.; Lindahl, P. A. *J. Am. Chem. Soc.* **2003**, *125*, 9316–9317.
(12) Seravalli, J.; Xiao, Y.; Gu, W.; Cramer, S. P.; Antholine, W. E.; Krymov, V.; Gerfen, G. J.; Ragsdale, S. W. *Biochemistry* **2004**, *43*, 3944–3955.
(13) Hegg, E. L. *Acc. Chem. Res.* **2004**, *37*, 775–783.
(14) Hatlevik, Ø.; Blanksma, M. C.; Mathrubootham, V.; Arif, A. M.; Hegg, E. L. *J. Biol. Inorg. Chem.* **2004**, *9*, 238–246.
(15) (a) Golden, M. L.; Rampersad, M. V.; Reibenspies, J. H.; Darensbourg, M. Y. *Chem. Commun.* **2003**, 1824–1825. (b) Rampersad, M. V.; Jeffery, S. P.; Golder, M. L.; Lee, J.; Reibenspies, J. H.; Darensbourg, D. J.; Darensbourg, M. Y. *J. Am. Chem. Soc.* **2005**, *127*, 17323–17334. (c) Golder, M. L.; Whaley, C. M.; Rampersad, M. V.; Reibenspies, J. H.; Hancock, R. D.; Darensbourg, M. Y. *Inorg. Chem.* **2005**, *44*, 875–883.
(16) (a) Wang, Q.; Blake, A. J.; Davies, E. S.; McInnes, E. J. L.; Wilson, C.; Schröder, M. *Chem. Commun.* **2003**, 3012–3013. (b) Duff, S. E.; Barclay, J. E.; Davies, S. C.; Evans, D. J. *Inorg. Chem. Commun.* **2005**, *8*, 170–173.
(17) (a) Evans, D. J. *Coord. Chem. Rev.* **2005**, *249*, 1582–1595. (b) Harrop, T. C.; Mascharak, P. K. *Coord. Chem. Rev.* **2005**, *249*, 3007–3024.
(18) Linck, R. C.; Spahn, C. W.; Rauchfuss, T. B.; Wilson, S. R. *J. Am. Chem. Soc.* **2003**, *125*, 8700–8701.
(19) (a) Harrop, T. C.; Olmstead, M. M.; Mascharak, P. K. *J. Am. Chem. Soc.* **2004**, *126*, 14714–14715. (b) Harrop, T. C.; Olmstead, M. M.; Mascharak, P. K. *Chem. Commun.* **2004**, 1744–1745. (c) Harrop, T. C.; Olmstead, M. M.; Mascharak, P. K. *Inorg. Chem.* **2006**, *45*, 3424–3436.
(20) (a) Krishnan, R.; Voo, J. K.; Riordan, C. G.; Zahkarov, L.; Rheingold, A. L. *J. Am. Chem. Soc.* **2003**, *125*, 4422–4423. (b) Krishnan, R.; Riordan, C. G. *J. Am. Chem. Soc.* **2004**, *126*, 4484–4485.
(21) (a) Rao, P. V.; Bhaduri, S.; Jiang, J.; Hong, D.; Holm, R. H. *J. Am. Chem. Soc.* **2005**, *127*, 1933–1945. (b) Rao, P. V.; Bhaduri, S.; Jiang, J.; Holm, R. H. *Inorg. Chem.* **2004**, *43*, 5833–5849.
(22) (a) Krüger, H.-J.; Holm, R. H. *Inorg. Chem.* **1987**, *26*, 3645–3647. (b) Krüger, H.-J.; Peng, G.; Holm, R. H. *Inorg. Chem.* **1991**, *30*, 734–742.
(23) Hanss, J.; Krüger, H.-J. *Angew. Chem., Int. Ed.* **1998**, *37*, 360–363.

leads to the formation of trinuclear or multinuclear complexes, although some success has been achieved using phosphine ligands.[16,19−21] Recently, binuclear Ni complexes containing a methylnickel moiety have been reported by Riordan and co-workers.[24] In addition, Tatsumi and co-workers[25] recently synthesized dinuclear models with exogenous monodentate thiolates and thiocarbamate ligands.

Interestingly, the active site of the enzyme Ni-superoxide dismutase[26] (Ni-SOD) (Figure 1B) resembles the $Ni^{II}N_2S_2$ coordination environment found in the distal nickel site of Ni-ACS. In the reduced state, the Ni^{II} ion exhibits a square-planar coordination geometry composed of two thiolates in a cis arrangement, a deprotonated amide nitrogen, and the terminal $-NH_2$ group. Ni-SOD catalyzes the disproportionation of superoxide to O_2 and H_2O_2, accessing both the Ni^{II} and Ni^{III} states during the catalytic cycle. An intriguing question concerning Ni-SOD is how the active-site avoids sulfur-based oxidation chemistry and performs Ni-based oxidation in the presence of superoxide, O_2, and H_2O_2 as reactants/products. Because Ni-bound thiolate groups are susceptible to modification and oxidation,[27−30] only a small number of synthetic Ni^{III} alkyl thiolate complexes have been reported thus far.[3,22,23,31] Holm[22] and Krüger[22,23] reported Ni^{III} complexes with thiolate ligation in the early to mid 1990s, one of which is the only Ni^{III} thiolate small molecule complex crystallographically characterized to date. Fiedler and Brunold[31] performed detailed spectroscopic/computational studies on these complexes, revealing important insight into the nature of $Ni^{III}-S$ bonding interactions. Significantly, recent work has demonstrated that NiN_2S_2 complexes in bisamine ligand environments are more stable toward O_2 than the corresponding bisamidate complexes.[14,28,29] It is also known that Ni^{III} is greatly stabilized by anionic amidate ligands relative to neutral amine ligands.[29,32] Thus, it is hypothesized that the mixed amine/amidate ligation utilized by Ni-SOD may allow the enzyme to stabilize the Ni^{III} state while at the same time avoiding sulfur-based oxidation.[32−34]

Relatively few examples of mixed amine/amidate nickel complexes have been reported as models for Ni-SOD.[34−38] Both Shearer[34] and others[35] have synthesized nickel-peptide complexes as functional models of Ni-SOD. The first synthetic mixed amine/amidate analogue of Ni-SOD was reported by Shearer and Zhao.[37] More recently, Grapperhaus and co-workers[38] reported a synthetic model with mixed amine/amidate ligation and imidazole ligation. Other models with a different ligand environment other than mixed amine/amidate have also been reported.[39] Interestingly, none of the synthetic analogues except the nickel-peptide models show SOD activity.

In this manuscript, we report the synthesis of related $Ni^{II}N_2S_2$ complexes, one with bisamidate ligation and the other with mixed amine/amidate ligation (Scheme 1). Because the ligands are identical except for a single amine/amidate, this study provides a unique opportunity to establish the role of the N donors in tuning the chemical and electrochemical properties in NiN_2S_2 complexes, to assess the importance of the N donors in controlling the reactivity of the metal center in these complexes, and to quantify the relative molecular orbital energies of amine/amidate versus bisamidate NiN_2S_2 complexes. Specifically, we prepared the Ni^{II} complex $((Ni^{II}(HL2))^-$ (**3**), which represents one of the very rare NiN_2S_2 model complexes containing Ni^{II} in a mixed amine/amidate environment. For comparison, we have also synthesized the analogous bisamidate complex, $(Ni^{II}(L1))^{2-}$ (**2**), which also provides information on whether the unsymmetrical orientation of amide carbonyl groups of the ligand backbone influences the properties of the Ni center. These complexes were probed using X-ray crystallography, electronic absorption spectroscopy, X-ray absorption spectroscopy, electron paramagnetic resonance (EPR) spectroscopy, and electrochemistry. Hybrid density functional theory (hybrid-DFT) and spectroscopy oriented configuration interaction (SORCI)

(24) Dougherty, W. G.; Rangan, K.; O'Hagan, M. J.; Yap, G. P. A.; Riordan, C. G. *J. Am. Chem. Soc.* **2008**, *130*, 13510–13511.

(25) (a) Ito, M.; Kotera, M.; Song, Y.; Matsumoto, T.; Tatsumi, K. *Inorg. Chem.* **2009**, *48*, 1250–1256. (b) Song, Y.; Ito, M.; Kotera, M.; Song, Y.; Matsumoto, T.; Tatsumi, K. *Chem. Lett.* **2009**, *38*, 184–185. (c) Ito, M.; Kotera, M.; Matsumoto, T.; Tatsumi, K. *Proc. Natl. Acad. Sci. U.S.A.* **2009**, *106*, 11862–11866.

(26) (a) Wuerges, J.; Lee, J.-W.; Yim, Y.-I.; Yim, H.-S.; Kang, S. −O.; Carugo, K. D. *Proc. Natl. Acad. Sci. U.S.A.* **2004**, *101*, 8569–8574. (b) Barondeau, D. P.; Kassmann, C. J.; Bruns, C. K.; Tainer, J. A.; Getzoff, E. D. *Biochemistry* **2004**, *43*, 8038–8047.

(27) (a) Grapperhaus, C. A.; Maguire, M. J.; Tuntulani, T.; Darensbourg, M. Y. *Inorg. Chem.* **1997**, *36*, 1860–1866. (b) Grapperhaus, C. A.; Darensbourg, M. Y. *Acc. Chem. Res.* **1998**, *31*, 451–459. (c) Kaasjager, V. E.; Bouwman, E.; Gorter, S.; Reedijk, J.; Grapperhaus, C. A.; Reibenspies, J. H.; Smee, J. J.; Darensbourg, M. Y.; Derecskei-Kovacs, A.; Thomson, L. M. *Inorg. Chem.* **2002**, *41*, 1837–1844. (d) Green, K. N.; Brothers, S. M.; Jenkins, R. M.; Carson, C. E.; Grapperhaus, C. A.; Darensbourg, M. Y. *Inorg. Chem.* **2007**, *46*, 7536–7544.

(28) Grapperhaus, C. A.; Mullins, C. S.; Kozlowski, P. M.; Mashuta, M. S. *Inorg. Chem.* **2004**, *43*, 2859–2866.

(29) Mullins, C. S.; Grapperhaus, C. A.; Kozlowski, P. M. *J. Biol. Inorg. Chem.* **2006**, *11*, 617–625.

(30) (a) Colpas, G. J.; Kumar, M.; Day., R. O.; Maroney, M. J. *Inorg. Chem.* **1990**, *29*, 4779–4788. (b) Mirza, S. A.; Pressler, M. A.; Kumar, M.; Day, R. O.; Maroney, M. J. *Inorg. Chem.* **1993**, *32*, 977–987. (c) Mirza, S. A.; Day, R. O.; Maroney, M. J. *Inorg. Chem.* **1996**, *35*, 1992–1995. (d) Chohan, B. S.; Maroney, M. J. *Inorg. Chem.* **2006**, *45*, 1906–1908.

(31) Fiedler, A. T.; Brunold, T. C. *Inorg. Chem.* **2007**, *46*, 8511–8521.

(32) (a) Fiedler, A. T.; Bryngelson, P. A.; Maroney, M. J.; Brunold, T. C. *J. Am. Chem. Soc.* **2005**, *127*, 5449–5462. (b) Margerum, D. W.; Anliker, S. L. In *The Bioinorganic Chemistry of Nickel*; Lancaster, J. R., Jr., Ed.; VCH: New York, 1988; pp 29−51. (c) Wang, J. F.; Kumar, K.; Margerum, D. W. *Inorg. Chem.* **1989**, *28*, 3481–3484. (d) Lappin, A. G.; Murray, C. K.; Margerum, D. .W. *Inorg. Chem.* **1978**, *17*, 1630–1634. (e) Bal, W.; Djuran, M. I.; Margerum, D. W.; Gray, E. T., Jr.; Mazid, M. A.; Tom, R. T.; Nieboer, E.; Sadler, P. J. *Chem. Commun.* **1994**, 1889–1890.

(33) It has been suggested by Darensbourg and co-workers that the kinetic control is responsible for preventing the sulfur oxygenation in the enzyme active site (ref 27d).

(34) (a) Shearer, J.; Long, L. M. *Inorg. Chem.* **2006**, *45*, 2358–2360. (b) Neupane, K. P.; Shearer, J. *Inorg. Chem.* **2006**, *45*, 10552–10556. (c) Neupane, K. P.; Gearty, K.; Francis, A.; Shearer, J. *J. Am. Chem. Soc.* **2007**, *129*, 14605–14618. (d) Shearer, J.; Neupane, K. P.; Callan, P. E. *Inorg. Chem.* **2009**, *48*, 10560–10571.

(35) (a) Schmidt, M.; Zahn, S.; Carella, M.; Ohlenschlager, O.; Gorlach, M.; Kothe, K.; Weston, J. *ChemBioChem* **2008**, *9*, 2135–2146. (b) Krause, M. E.; Glass, A. M.; Jackson, T. A.; Laurence, J. S. *Inorg. Chem.* **2010**, *49*, 362–364.

(36) Tietze, D.; Breitzke, H.; Imhof, D.; Kothe, E.; Weston, J.; Buntkowsky, G. *Chem.—Eur. J.* **2009**, *15*, 517–523.

(37) (a) Shearer, J.; Zhao, N. *Inorg. Chem.* **2006**, *45*, 9637–9639. (b) Shearer, J.; Dehestani, A.; Abanda, F. *Inorg. Chem.* **2008**, *47*, 2649–2660.

(38) Mullins, C. S.; Grapperhaus, C. A.; Frye, B. C.; Wood, l. H.; Hay, A. J.; Buchanan, R. M.; Mashuta, M. S. *Inorg. Chem.* **2009**, *48*, 9974–9976.

(39) Recently, Darensbourg and co-workers and Harrop and co-workers prepared models with imidazole and pyridine ligations, respectively, to model the histidine ligation of the Ni-SOD, while Jenson and co-workers synthesized models with trispyrazolyl tripodal ligand and thiocabamate ligands. (a) Jenkins, R. M.; Singleton, M. L.; Almaraz, E.; Reibenspies, J. H.; Darensbourg, M. Y. *Inorg. Chem.* **2009**, *48*, 7280–7293. (b) Gale, E. M.; Patra, A. K.; Harrop, T. C. *Inorg. Chem.* **2009**, *48*, 5620–5622. (c) Ma, H.; Chattopadhyay, S.; Petersen, J. L.; Jensen, M. P. *Inorg. Chem.* **2008**, *47*, 7966–7968. (d) Ma, H.; Wang, G.; Yee, G. T.; Petersen, J. L.; Jensen, M. P. *Inorg. Chim. Acta* **2009**, *362*, 4563–4569.

Scheme 1. Structures of Ligands

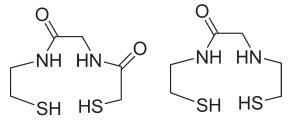

$H_4(L1)$ $H_4(L2)$

calculations were performed to explain the experimentally observed properties. These results and their implications with respect to the possible role of mixed amine/amidate ligation in Ni-SOD are discussed.

Experimental Section

General Methods. Solvents were purified according to standard procedures and were freshly distilled under N_2 atmosphere prior to use. All chemicals/solvents were obtained from Aldrich or Acros Organics unless otherwise noted. All air-sensitive chemical manipulations were performed in a glovebox under an atmosphere of N_2 or using standard Schlenk-line techniques under an Ar atmosphere. The ligand *N*-(2-mercaptoacetyl)-*N*′-(2-mercaptoethyl)glycinamide H_4(L1) was synthesized according to literature procedure.[40a]

Physical Methods. Optical spectra were obtained on a Hewlett-Packard 8453 diode array spectrophotometer. Electrochemistry was performed under anaerobic conditions in dimethylformamide (DMF) on a BAS CV-50W voltammetric analyzer using the following conditions: ~1 mM sample, 100 mV/s scan rate, 0.1 M *N*-tetrabutylammonium perchlorate (TBAP) as supporting electrolyte, Pt disk working electrode, Ag/Ag^+ (0.01 M $AgNO_3$/0.1 M TBAP in CH_3CN) reference electrode, and Pt counter electrode. Ferrocene was used as a standard, and all potentials are reported relative to NHE ($Fc/Fc^+ = +0.720$ V versus NHE in DMF[41]). Under our experimental conditions, the potential for the Fc/Fc^+ couple was +0.083 V versus Ag/Ag^+ reference electrode. NMR spectra were recorded on a Varian 300 MHz spectrometer at the NMR facility, Department of Chemistry, Michigan State University.

The EPR data were collected on a Bruker ESP-300E X-band EPR spectrometer using an ST4102 cavity resonator. The sample temperature was maintained at 10 K using an Oxford ESR-900 liquid helium cryostat system equipped with an ITC-502 temperature controller. The microwave frequency was measured with an EIP model 25B frequency counter, and the magnetic field was calibrated using weak pitch as the standard. Conditions for the EPR measurement: microwave frequency, 9.4628 GHz; microwave power, 0.2 mW; field modulation, 0.8 mT at 100 kHz; time constant, 163 ms; receiver gain, 1.0×10^6; scans averaged, 4; sample temperature, 10 K.

Synthesis. *N*-(2″-Mercaptoethyl)-2-[(2′-mercaptoethyl)amino]-acetamide, H_4L2. This ligand was synthesized as the trifluoroacetate salt in three steps using modified literature procedures.[40b,c]

Step 1. Preparation of *N*-(2-Bromoacetyl)-*S*-(triphenylmethyl)-2-aminoethanethiol. A solution of bromoacetic acid (1.39 g, 10 mmol) in CH_2Cl_2 (25 mL) was treated with *N*-methylmorpholine (15 mmol, 1.70 mL) and cooled to −15 °C (salt-ice bath). After dropwise addition of isobutylchloroformate (11.5 mmol, 1.5 mL), the resulting mixture was stirred for 10 min at −15 °C. A slurry of 2-(triphenylmethythio)ethylamine (11.5 mmol, 3.70 g) in 25 mL of CH_2Cl_2 was added at −15 °C in 5 aliquots to the reaction mixture. The solution was warmed to +15 °C over an hour, diluted with 200 mL of CH_2Cl_2, washed with 1 M HCl (100 mL), H_2O (100 mL), and brine (100 mL), dried (Na_2SO_4), and concentrated via rotary evaporation. A sticky foam-like material was obtained, and this material was dried under vacuum. Yield. 3.72 g, 85%.

Step 2. Preparation of *N*-[2-(2-Triphenlmethylthio)ethyl)amino)-acetyl]-*S*-(triphenylmethyl)-2-aminoethanethiol. *N*-(2-Bromoacetyl)-*S*-(triphenylmethyl)-2-aminoethanethiol was converted to *N*-[2-(2-triphenlmethylthio)ethyl)amino)acetyl]-*S*-(triphenylmethyl)-2-aminoethanethiol using a previously reported procedure.[40b]

Step 3. Ligand H_4L2. Triethylsilane (2−3 mL) was added to a solution of *N*-[2-(2-triphenylmethylthio)ethyl)amino)acetyl]-*S*-(triphenylmethyl)-2-aminoethanethiol (3.40 g, 5 mmol) in trifluoroacetic acid (30 mL) cooled in an ice bath. A bright yellow color formed initially followed by the formation a white precipitate. The mixture was diluted with hexanes (50 mL) and water (50 mL), and the aqueous phase was separated, washed with several portions of hexanes, and evaporated to a colorless oil. The oil was triturated with diethyl ether to yield a white solid (trifluoroacetate salt) that was collected, washed with ether, and dried in vacuo. Yield.1.49 g, 96.8%, ^{1}H NMR (DMSO-d_6): δ 2.58 (m, 2H, CH_2) merged with residual solvent peak, 2.74 (t, 2H, CH_2), 3.13 (t, 2H, CH_2), 3.32 (q, 2H, CH_2), 3.78 (s, 2H, CH_2), 8.68 (t, 1H, NH), 9.02 (br, 2H, NH_2).

Preparation of $(Et_4N)_2(\{Ni(L1)\}_2Ni)\cdot H_2O$ (1). NaOMe (2.27 g, 42 mmol) in 20 mL of CH_3OH was added to a solution of ligand H_4L1 (2.08 g, 10 mmol) in 20 mL of CH_3OH. To the clear yellow solution was added a methanolic solution (5 mL) of Et_4NCl (3.31 g, 20 mmol) resulting in the appearance of a turbid yellow solution. The solution was stirred for 30 min followed by the dropwise addition of $Ni(OAc)_2.4H_2O$ (2.49 g, 10 mmol) in 50 mL of CH_3OH. The initial pale yellow color of the solution changed to red and then to brownish green. This mixture was allowed to stir for 2 h, and the solvent was removed in vacuo. The residue was extracted with CH_3CN, and the extract was filtered, concentrated, and layered with diethyl ether to cause the formation of green crystals. Yield: 0.482 g (17% based on Ni). (ESI^-): (*m*/*z*) 713.9 $[M - Et_4N]^-$.

Preparation of the Mononuclear Complex $(Et_4N)_2(Ni(L1))\cdot 2H_2O$ (2). NaOMe (0.24 g, 4.4 mmol) in 5 mL of CH_3OH was added to a solution of H_4L1 (0.028 g, 0.132 mmol) in 20 mL of CH_3OH. This mixture was slowly added to a green solution of **1** (0.1 g, 0.12 mmol) in 50 mL of CH_3CN resulting in the formation of a red solution. The reaction mixture was stirred for 10 min, and a solution of Et_4NCl (0.08 g, 0.48 mmol) in CH_3CN (10 mL) was added, resulting in the precipitation of NaCl. The mixture was stirred for 30 min, and the solvent was evaporated to dryness. The red solid was extracted with CH_3CN, and the extract was filtered and layered with diethyl ether to obtain red crystals. The crystals were filtered and washed with diethyl ether. Yield.0.094 g (47% based on Ni). ^{1}H NMR δ 1.30 (t-t, 24H, tetraethylammonium cation-CH_3), 2.02 (t, 2H, CH_2), 2.56 (s, 2H, CH_2), 2.78 (t, 2H, CH_2), 3.26 (s, 2H, CH_2), 3.40 (q, 12H, tetraethylammonium cation-CH_2); MS (ESI^-): (*m*/*z*) 392.1 $[M - Et_4N]^-$.

Preparation of K(Ni(HL2)) (3). KOH (1.40 g, 25 mmol) in 20 mL of CH_3OH was added to a solution of ligand H_4L2 (1.54 g, 5 mmol) in 20 mL of CH_3OH. The solution was stirred for 30 min followed by the dropwise addition of a solution of $Ni(OAc)_2\cdot 4H_2O$ (1.25 g, 5 mmol) in 50 mL of CH_3OH. The solution changed to red immediately and then reddish brown. This mixture was allowed to stir for 2 h, and the solvent was removed in vacuo. The resulting residue was dissolved in 50:50 CH_3OH/CH_3CN, filtered, and layered with diethyl ether resulting in the formation of red crystals. Yield. 1.1 g (75.9%) ^{1}NMR (DMSO-d_6): δ 1.74 (t, 2H, CH_2), 1.84 (t, 2H, CH_2), 2.38 (t, 2H, CH_2) br, 2.66 (t, 2H, CH_2) br, 2.96 (s, 2H, CH_2). MS (ESI^-): (*m*/*z*) 248.9 $[M - K]^-$. The same cationic potassium complex was obtained even in the presence of Et_4NCl, as confirmed by NMR and X-ray crystallography.

(40) (a) Brenner, D.; Davison, A.; Lister-James, J.; Jones, A. G. *Inorg. Chem.* **1984**, *23*, 3793–3797. (b) O'Neil, J. P.; Wilson, S. R.; Katzenellenbogen, J. A. *Inorg. Chem.* **1994**, *33*, 319–323. (c) Oya, S.; Plössl, K.; Kung, M.-P.; Stevenson, D. A.; Kung, H. F. *Nucl. Med. Biol.* **1998**, *25*, 135–140.

(41) Barrette, W. C., Jr.; Johnson, H. W., Jr.; Sawyer, D. T. *Anal. Chem.* **1984**, *56*, 1890–1898.

Table 1. Details of Structure Determination, Refinement, and Experimental Parameters for Compounds **1**, **2**, and **3**

	1	**2**	**3**
chemical formula	$C_{28}H_{58}N_6Ni_3O_5S_4$	$C_{22}H_{52}N_4NiO_4S_2$	$C_6H_{11}KN_2NiOS_2$
formula weight	863.17	559.51	289.10
crystal system	monoclinic	orthorhombic	monoclinic
space group	$P2_1/c$	$Pna2_1$	$P2_1/c$
a (Å)	13.0861(4)	14.3804(4)	8.5857(2)
b (Å)	9.7990(3)	13.8008(4)	11.6498(3)
c (Å)	28.5967(9)	14.2473(3)	11.2093(3))
α (deg)	90	90	90
β (deg)	90.078(2)	90	111.7573(15)
γ (deg)	90	90	90
V (Å^3)	3667.0(2)	2827.53(13)	1041.30(5)
Z	4	4	4
μ(Mo Kα) (mm^{-1})	1.797	0.867	2.624
crystal size (mm)	0.36 × 0.34 × 0.08	0.363 × 0.332 × 0.233	0.25 × 0.20 × 0.13
F (000)	1824	1216	592
2θ range (deg)	1.56 to 25.36	2.05 to 25.34	2.55 to 27.46
T (K)	173(2)	173(2)	150(1)
number of data collected	39471	15683	4414
number of unique data	6687	5042	2371
observed data [$I > 2\sigma(I)$]	5713	4464	2042
R_{int} (%)	4.40	6.08	1.80
number of parameters	435	307	158
$R1$ (%)[a]	3.46	3.70	3.35
$wR2$ (%)[b]	6.87	8.68	8.18
S[c]	1.072	0.992	1.040
$\Delta\rho_{min}$ (e$^-$ Å^{-3})	−0.326	−0.260	−0.756
$\Delta\rho_{max}$ (e$^-$ Å^{-3})	0.495	0.984	0.846

[a] $R1 = \sum||F_o| - |F_c||/\sum|F_o|$. [b] $wR_2 = \{\sum[w(F_o^2 - F_c^2)^2/\sum[w(F_o^2)^2]\}^{1/2}$. [c] Goodness-of-fit on $F^2 = [\sum[w(F_o^2 - F_c^2)^2]/(n-p)]^{1/2}$, where n is the number of reflections and p is the number of parameters refined.

X-ray Structure Determination. A green hexagonal plate crystal of **1** with dimensions 0.08 × 0.34 × 0.36 mm was mounted on a Nylon loop using a very small amount of paratone oil. Data were collected using a Bruker CCD (charge coupled device) based diffractometer equipped with an Oxford Cryostream low-temperature apparatus operating at 173 K. Data were measured using ω and φ scans of 0.5° per frame for 30 s. The total number of images was based on results from the program COSMO[42] where redundancy was expected to be 4.0 and completeness of 100% out to 0.83 Å. Cell parameters were retrieved using APEX II software[43] and refined using SAINT on all observed reflections. Data reduction was performed using the SAINT software[44] which corrects for Lorentz-polarization. Scaling and absorption corrections were applied using SADABS[45] multiscan technique, supplied by George Sheldrick. The structures were solved by the direct method using the SHELXS-97 program and refined by least-squares method on F^2, SHELXL-97, incorporated in SHELXTL-PC V 6.10.[46] The structure was solved in the space group $P2_1/c$. All non-hydrogen atoms were refined anisotropically. Hydrogens were calculated by geometrical methods and refined as a riding model. The twin law was applied and refined to a value of 0.262 for the twin law matrix [1 0 0, 0 −1 0, 0 0 −1]. Crystallographic summary of data and selected experimental information is given in Table 1, and selected bond lengths and angles are given in Table 2.

A red block crystal of **2** with dimensions 0.36 × 0.33 × 0.23 mm was mounted on a Nylon loop using a very small amount of paratone oil. The data collection was performed using the same instrument and methods as described for **1**. The structure was solved in the orthorhombic space group $Pna2_1$. All non-hydrogen atoms were refined anisotropically. Hydrogens were calculated by geometrical methods and refined as a riding model. The Flack[47] parameter was used to determine chirality of the crystal studied. A value of zero or one indicates that the crystal is composed of a single enantiomer, while a value of 0.5 indicates a racemic crystal. The Flack parameter was refined by use of the twin law to 0.456(12), indicating a racemic crystal.

A red prism-shaped crystal of **3** with dimensions 0.25 × 0.20 × 0.13 mm was mounted on a glass fiber with traces of viscous oil and then transferred to a Nonius Kappa CCD diffractometer equipped with Mo Kα radiation (λ = 0.71073 Å). Ten frames of data were collected at 150(1) K with an oscillation range of 1 deg/frame and an exposure time of 20 s/frame.[48] Indexing and unit cell refinement based on all observed reflection from those 10 frames indicated a monoclinic P lattice. A total of 4414 reflections (Θ_{max} = 27.46°) were indexed, integrated, and corrected for Lorentz-polarization and absorption effects using DENZO-SMN and SCALEPAC.[49] Post refinement of the unit cell gave a = 8.5857(2) Å, b = 11.6498(3) Å, c = 11.2093(3) Å, and V = 1041.30(5) Å^3. Axial photographs and systematic absences were consistent with the compound having crystallized in the monoclinic space group $P2_1/c$. The structure was solved by a combination of direct methods and heavy atom using SIR 97.[50] All of the non-hydrogen atoms were refined with anisotropic displacement coefficients. Hydrogen atoms were either located and refined isotropically or were assigned isotropic displacement coefficients U(H) = 1.2U(C), and their coordinates were allowed to ride on their respective carbons using SHELXL-97.[51] The

(42) *COSMO V1.56, Software for the CCD Detector Systems for Determining Data Collection Parameters* ; Bruker Analytical X-ray Systems: Madison, WI, 2006.
(43) *APEX2 V 1.2-0 Software for the CCD Detector System*; Bruker Analytical X-ray Systems, Madison, WI, 2006.
(44) *SAINT V 7.34 Software for the Integration of CCD Detector System*; Bruker Analytical X-ray Systems: Madison, WI, 2001.
(45) *SADABS V2.10 Program for absorption corrections using Bruker-AXS CCD based on the method of Robert Blessing*; Blessing, R. H. *Acta Crystallogr.* **1995**, *A51*, 33−38.
(46) Sheldrick, G. M. *Acta Crystallogr.* **2008**, *A64*, 112-122.
(47) Flack, H. D. *Acta Crystallogr.* **1983**, *A39*, 876–881.
(48) *COLLECT Data Collection Software*; Nonius B.V.: Delft, The Netherlands, 1998.
(49) Otwinowski, Z.; Minor, W. *Methods Enzymol.* **1997**, *276*, 307–326.
(50) Altomare, A.; Burla, M.C.; Camalli, M.; Cascarano, G.; Giacovazzo, C.; Guagliardi, A.; Moliteni, A.G. G.; Polidori, G.; Spagna, R. *SIR97 (Release 1.02) - A program for automatic solution and refinement of crystal structure.*

Table 2. Selected Bond Lengths (Å) and Angles (deg) for the Anionic Complexes $(\{Ni^{II}(L1)\}_2Ni^{II})^{2-}$ (**1**), $(Ni^{II}(L1))^{2-}$ (**2**), and $(Ni^{II}(HL2))^{-}$ (**3**)

	1	2	3
Ni(1)−N(1)	1.846(3)	1.858(3)	1.862(2)
Ni(1)−N(2)	1.841(4)	1.874(3)	1.937(3)
Ni(1)−S(1)	2.1504(12)	2.1812(10)	2.1671(8)
Ni(1)−S(2)	2.1405(11)	2.1886(9)	2.1711(7)
Ni(2)−S(1)	2.2420(10)		
Ni(2)−S(2)	2.2419(10)		
N(1)−Ni(1)−N(2)	86.11(15)	84.96(12)	84.46(12)
N(1)−Ni(1)−S(1)	91.19(11)	173.44(9)	89.57(7)
N(2)−Ni(1)−S(1)	168.46(11)	88.57(9)	172.37(10)
N(1)−Ni(1)−S(2)	169.27(11)	87.87(8)	174.78(8)
N(2)−Ni(1)−S(2)	90.80(11)	172.68(9)	90.62(9)
S(2)#1−Ni(1)−S(1)	89.80(4)		
N(2)−Ni(1)−Ni(2)	118.79(11)		
N(1)−Ni(1)−Ni(2)	119.62(10)		

nitrogen atom N2 exhibits orientation disorder into two sites (75:25). The weighting scheme employed was $w = 1/[\sigma^2(F_o^2) + (0.0379P)^2 + 1.7429P]$ where $P = (F_o^2 + 2F_c^2)/3$. The refinement converged to R1 = 0.0335, wR2 = 0.0818, and $S = 1.04$ for 2042 reflections with $I > 2\sigma(I)$, and R1 = 0.0419, wR2 = 0.0859, and $S = 1.04$ for 2371 unique reflections and 158 parameters.[52]

Sulfur K-edge X-ray Absorption Spectroscopy. The nickel complexes $(Ni^{II}(L1))^{2-}$ (**2**) and $(Ni^{II}(HL2))^{-}$ (**3**) were finely ground under an atmosphere of N_2, and the powders were spread onto sulfur-free Kapton tape (verified by scanning the tape over the energy region used in this study) forming thin layers. These samples were then mounted onto polycarbonate sample holders. Data were collected at room temperature on beamline X19A at the National Synchrotron Light Source (Brookhaven National Laboratories; Upton, NY). Spectra were recorded in fluorescence mode using a passivated implanted planar silicon detector (Canberra Industries). The X-ray beam passed from an incident ionization chamber to the sample chamber, which were both continually purged with He and separated from one another by polyethylene windows (5 μm thickness). Data were collected from 200 eV below the edge to 300 eV above the edge. In the pre-edge region (2270−2465 eV), data were collected in 5 eV steps; in the edge region (2465−2475 eV), data were collected in 0.1 eV steps, and in the near edge region (2475−2765 eV) data were collected in 0.5 eV steps. All spectra were calibrated against the spectrum of Na_2SO_4, which was independently recorded in between each scan. The energy drifted by less than 0.1 eV from scan to scan. All reported spectra represent the average of 5 scans.

Data were averaged and a baseline was applied to each spectrum by fitting the pre-edge region to a polynomial function. This baseline was then subtracted from the whole spectrum. The region above the edge jump was fit to a two knot cubic spline and the data normalized to the edge height. Pre-edge and the rising-edge features were modeled as pseudo-Voigt line shapes (a 1:1 sum of Gaussian and Lorentzian line shapes). Each spectrum required the use of only one peak per feature, and valid fits to the data were judged by matches to the second derivatives of the spectra. The intensity values of the pre-edge features, which represent the average of four different fits to the data (differing by less than 2%), are the products of the peak widths at half height and intensities of the pseudo-Voigt line shapes. All pre-edge intensities were then converted into %S(3p) character using the pre-edge feature of Ni(DACO) as a standard (46(2)%),[53] which by our fitting procedure corresponds to an intensity of 1.22(1) units.

77 K Electronic Absorption Spectroscopy. Under an atmosphere of N_2, solids of the monomeric $Ni^{II}N_2S_2$ compounds were finely ground in Nujol and placed between two quartz plates. The plates were then mounted in a custom-built low-temperature optical cryostat, which was cooled to 77 K. Data were then recorded on an OLIS-CARY 14. Each spectrum represents the average of 5 scans. Data were deglitched and smoothed prior to examining the second derivative of the averaged spectra. The resulting transitions were deconvoluted into four Gaussian line shapes (Supporting Information, Table S13). The TT-multiplets software package was then used to generate correlation diagrams for Ni^{II} contained within D_{4h} symmetry using previously determined values for $10D_q$, D_s, and D_t to allow for a fitting of the resulting Slater−Condon parameters.[37,54]

Electronic Structure Calculations. All electronic structure and excited-state calculations were performed using the software package ORCA 2.6.35.[55] All calculations on $S = 0$ Ni^{II} complexes were spin-restricted and all calculation on low-spin $S = 1/2$ Ni^{III} complexes were spin-unrestricted. Geometry-optimized (GO) structures were obtained for all complexes starting from the available X-ray crystallographic coordinates of the reduced Ni^{II} compounds, and utilized the following thresholds in the GO procedure (in au): root-mean square (rms) and maximum forces of 0.00003 and 0.0001, respectively; rms and maximum gradients 0.002 and 0.0003, respectively. These calculations utilized Becke's three-parameter hybrid functional for exchange along with the Lee−Yang−Parr correlation functional (B3LYP),[56] and utilized Ahlrichs' triple-ζ valence basis set with one set of first polarization functions (TZVP).[57] All geometry-optimized structures were subjected to vibrational analyses to ensure only real vibrational modes were present. Single-point calculations also utilized the B3LYP functional, but all atoms were treated with Ahlrichs' triple-ζ valence basis set with two sets of first polarization functions (TZVPP)[57] except Ni, S, and N, which were treated with Ahlrichs' def2 triple-ζ valence basis set with two sets of first polarization functions and diffuse functions (Def2-aug-TZVPP).[57,58] Iso-surface plots were generated with the visualization package gOpenMol[59a,b] or Molekel.[59c] All population analyses were performed within ORCA 2.6.35 and are reported to the nearest 0.1%. Löwdin populations are reported in the text of the manuscript while Mulliken populations are reported in the Supporting Information and ref 66 for comparative purposes. Excited-state calculations were performed using the spectroscopy oriented configuration interaction (SORCI) formalism of Neese.[60] These calculations employed Ahlrichs' Def2-aug-TZVPP basis-set on all atoms.[56,57] For the SORCI calculations, the selection threshold was set to 10^{-6} E_h, the prediagonalization threshold was set to 10^{-6}, and the natural orbital threshold was set to 10^{-5}. All orbitals between −3 to 5 E_h of the highest occupied molecular

(51) Sheldrick, G. M. *SHELX97* [*Includes SHELXS97, SHELXL97, CIFTAB*] - *Programs for Crystal Structure Analysis* (*Release 97−2*); University of Göttingen: Göttingen, Germany, 1997.

(52) R1 = $\sum||F_o| - |F_c||/\sum|F_o|$, wR2 = $[\sum w(F_o^2 - F_c^2)^2/\sum w(F_o^2)^2]^{1/2}$, and S = Goodness-of-fit on $F^2 = [\sum[w(F_o^2 - F_c^2)^2]/(n-p)]^{1/2}$, where n is the number of reflections and p is the number of parameters refined.

(53) Dey, A.; Jeffery, S. P.; Darensbourg, M.; Hodgson, K. O.; Hedman, B.; Solomon, E. I. *Inorg. Chem.* **2007**, *46*, 4989–4996.

(54) (a) de Groot, F. M. F. *J. Electron Spectrosc. Relat. Phenom.* **1994**, *67*, 529–622. (b) de Groot, F. M. F. *Chem. Rev.* **2001**, *101*, 1779–1808.

(55) Neese, F. *ORCA Version 2.6.35*; Universitat Bonn: Bonn, Germany, 2008.

(56) (a) Becke, A. D. *J. Chem. Phys.* **1993**, *98*, 5648–5652. (b) Becke, A. D. *J. Chem. Phys.* **1993**, *98*, 1372–1377. (c) Lee, C. T.; Yang, W. T.; Parr, R. G. *Phys. Rev. B: Condens. Matter* **1988**, *37*, 785–789.

(57) (a) Schäfer, A.; Horn, H.; Ahlrichs, R. *J. Chem. Phys.* **1992**, *97*, 2571–2577. (b) Ahlrichs, R. and coworkers, unpublished work.

(58) (a) Dunning, T. H., Jr. *J. Chem. Phys.* **1989**, *90*, 1007–1023. (b) Woon, D. E.; Dunning, T. H., Jr. *J. Chem. Phys.* **1994**, *100*, 2975–2988. (c) Woon, D. E.; Dunning, T. H., Jr. *J. Chem. Phys.* **1993**, *98*, 1358–1371.

(59) (a) Bergman, D. L.; Laaksonen, L.; Laaksonen, A. *J. Mol. Graphics Modell.* **1997**, *15*, 301–306. (b) Laaksonen, L. *J. Mol. Graphics* **1992**, *10*, 33–34. (c) Varetto, U. *Molekel v. 5.4*; Swiss National Supercomputing Center: Manno, Switzerland.

(60) Neese, F. *J. Chem. Phys.* **2003**, *119*, 9428–9443.

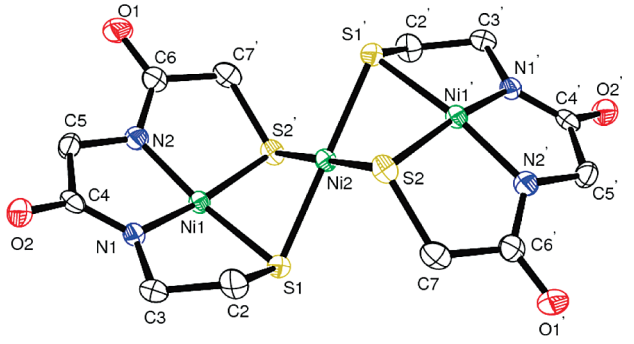

Figure 2. ORTEP view of $[Ni\{Ni(L1)\}_2]^{2-}$ (anion of **1**) showing 50% probability displacement ellipsoids. H atoms, counterions, and solvent molecules are not shown.

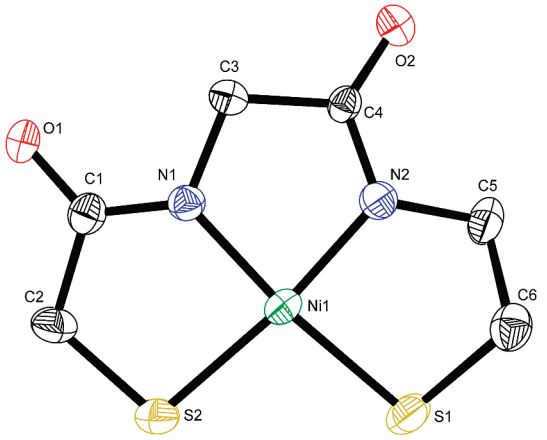

Figure 3. ORTEP view of $[Ni(L1)]^{2-}$ (anion of **2**) showing 50% probability displacement ellipsoids. H atoms, counterions, and solvent molecules are not shown.

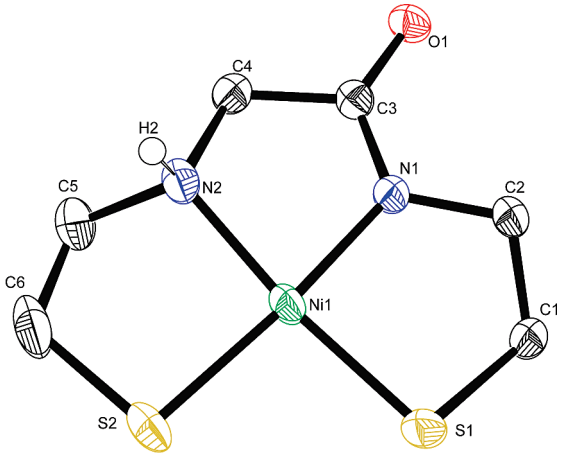

Figure 4. ORTEP view of $[Ni(HL2)]^-$ (anion of **3**) showing 50% probability displacement ellipsoids. H atoms, counterions, and solvent molecules are not shown.

orbital (HOMO)/lowest unoccupied molecular orbital (LUMO) gap were considered in the SORCI treatment. In addition, the CAS-SCF(12,7) reference space was used,[61] and we examined the first seven spin allowed excitations.[62] EPR *g*-values and superhyperfine coupling constants were calculated by solving the coupled-perturbed SCF equations,[63] using the B3LYP functional, the TZVP basis-set for all non-ligating atoms, the Def2-aug-TZVPP basis set for Ni and S, and Kutzelnigg's IGLO III basis set for ligated N atoms.[64] All orbitals from −100 to 100 E_h of the HOMO/LUMO gap were considered, with the center of electronic charge defined as the origin of the *g*-matrix.

Results

Synthesis. The deprotonation of the ligand H_4L1 with 4 equiv of NaOMe, followed by the addition of 1 equiv of $Ni(acetate)_2 \cdot 4H_2O$ afforded the green trinuclear complex $(\{Ni^{II}(L1)\}_2Ni^{II})^{2-}$ (**1**) which was isolated as the Et_4N^+ salt. The desired mononuclear bisamidate complex $(Ni^{II}(L1))^{2-}$ (**2**) was obtained as the Et_4N^+ salt by breaking apart the trinuclear complex **1** by the addition of 1 equiv of the ligand H_4L1 and 4 equiv of NaOMe. The red mixed amine/amidate complex $(Ni^{II}(HL2))^-$ (**3**) was prepared by deprotonating the ligand H_4L2 using KOH, followed by the addition of $Ni(acetate)_2 \cdot 4H_2O$ in CH_3OH and isolated as the K^+ salt.

X-ray Crystal Structure Descriptions. The Oak Ridge thermal ellipsoid plot (ORTEP) of complexes **1**, **2**, and **3** is shown in the Figures 2, 3, and 4, respectively, and the selected bond lengths and angles are given in Table 2. Complexes **1** and **3** crystallize in the monoclinic space group $P2_1/c$ while complex **2** crystallizes in the orthorhombic space group $Pna2_1$ with two independent molecules in the same asymmetric unit. The overall geometry of the trinuclear anion of **1** can be described as a chair consisting of three square planes in which a central Ni ion sits at an inversion center and bridges two anionic bisamidate complexes (**2**). The dihedral angle formed between these planes is 111.4°, although the deviation from the NiN_2S_2 least-squares planes is appreciable for Ni (0.404 Å), C2 (0.609 Å), C6 (0.305 Å), and C7 (0.420 Å). In one of the trimers in the asymmetric unit, all of the Ni−S distances in the NiS_4 plane refine to the same value by coincidence, while in the second molecule the two independent Ni−S distances are slightly different. In both molecules of the asymmetric unit, the Ni−S bond lengths in the NiS_4 plane are similar to those reported by us[14] and others.[16b,19b,19c,21] Conversely, while the Ni−S bond lengths in the NiN_2S_2 planes are similar to ($\{Ni(ema)\}_2Ni$),[16b] where ema = *N*,*N*′-ethylenebis-2-mercaptoacetamide, they are significantly lower than in the 6,5,6 chelated bis[Ni^{II}*N*,*N*′-ethylenebis(3-mercaptopropionamide)]Ni^{II} trimer complex[14] and the 6,5,5 chelating ring complex reported by Holm.[21b]

In the mononuclear bisamidate complex $(Ni^{II}(L1))^{2-}$ (**2**), the asymmetric unit contains a nickel coordinated by two amido nitrogens and two thiolate sulfurs in a square-planar environment. The Ni−N bond distances are in the range for Ni−N amidate bonds in square-planar complexes.[14,17b,21−23] Likewise, the Ni−S distances are in the range of other NiN_2S_2 square-planar thiolate complexes.[14,17b,21−23] Interestingly, the asymmetrically positioned carbonyl groups

(61) CAS(*n*,*m*): complete active space composed of *n* electrons in *m* orbitals; for this case we consider the LUMO through HOMO-6 in our reference space.

(62) Expanding the reference space does not in general lead to an improvement in calculated transitions energies or strengths for the lowest energy transitions in similar $Ni^{II}N_2S_2$ complexes. Shearer, J., unpublished results.

(63) (a) Neese, F. *J. Chem. Phys.* **2001**, *115*, 11080–11096. (b) Neese, F. *Curr. Opin. Chem. Biol.* **2003**, *7*, 125–135.

(64) Kutzelnigg, W.; Fleischer, U.; Schindler, M. The IGLO-Method: Ab-initio Calculation and Interpretation of NMR Chemical Shifts and Magnetic Susceptibilities. In *NMR, Basic Principles and Progress*; Diehl, P., Fluck, E., Günther, H., Kosfield, R., Seelig, J., Eds.: Springer Verlag: Berlin, 1990; Vol. *23*, pp 165−262.

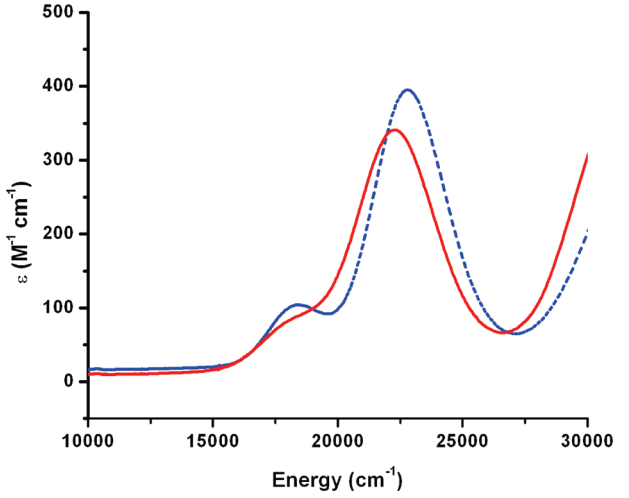

Figure 5. Room temperature electronic absorption spectra of $[Ni^{II}(L1)]^{2-}$ (**2**) (dashed blue line) and $[Ni^{II}(HL2)]^{-}$ (**3**) (solid red line) in methanol.

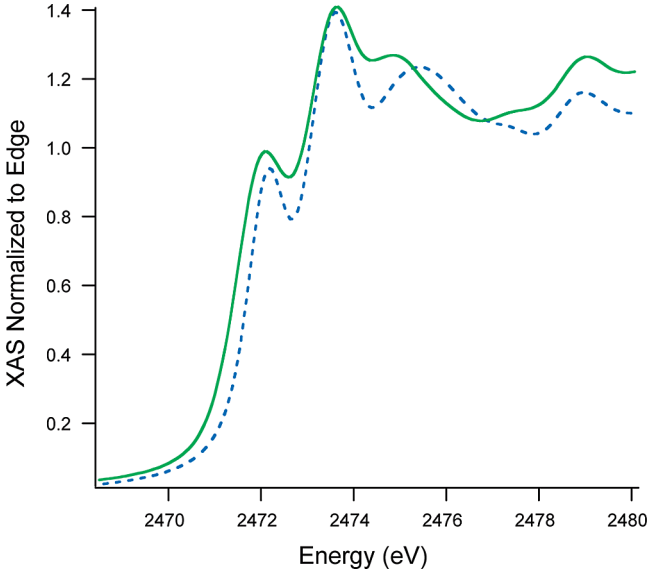

Figure 6. Sulfur K-edge X-ray absorption spectra of $(Ni^{II}(L1))^{2-}$ (**2**) (dashed blue line) and $(Ni^{II}(HL2))^{-}$ (**3**) (solid green line). There is a shift in the pre-edge feature of $(Ni^{II}(HL2))^{-}$ (**3**) versus $(Ni^{II}(L1))^{2-}$ (**2**) to higher energy by ~0.3 eV.

in the ligand backbone impose slight differences in the bond lengths and angles compared to the analogous symmetric 5,5,5 chelate ring NiN_2S_2 square-planar bisamidate complex previously reported.[14,22b]

The X-ray structure of the mixed amine/amidate complex $(Ni^{II}(HL2))^{-}$ (**3**) reveals a nickel ion in a square-planar coordination geometry, with the plane defined by two thiolato sulfurs, one carboxamido nitrogen, and an amine nitrogen. The Ni ion deviates from the least-squares N_2S_2 plane by only 0.097 Å. Predictably, the Ni−N (amide) distance (Ni1−N1, 1.862(2) Å) is shorter than the Ni−N(amine) (Ni1−N2, 1.937(3) Å) distance. As expected, the Ni−S bond (Ni−S1, 2.1671(8) Å) trans to the amine N is slightly shorter than the Ni−S bond (Ni−S2, 2.1711(7) Å) trans to the amidate N because N(amide) ligands are stronger σ donors than N(amine) ligands and display more trans influence. The difference, however, is not appreciable.

Room Temperature Solution Electronic Absorption Properties. The trinuclear complex $(\{Ni^{II}(L1)\}_2Ni^{II})^{2-}$ (**1**) displays two absorption bands at 21,881 cm^{-1} (8400 M^{-1} cm^{-1}) and 14,749 cm^{-1} (9600 M^{-1} cm^{-1}) in CH_3CN similar to the other reported trinuclear NiN_2S_2 complexes.[14−23] The UV−vis absorption spectrum of complex $(Ni^{II}(L1))^{2-}$ (**2**) in CH_3OH (Figure 5) exhibits two ligand field transitions at 22,779 cm^{-1} (400 M^{-1} cm^{-1}) and 18,382 cm^{-1} (100 M^{-1} cm^{-1}), which is typical for Ni^{II} complexes with dicarboxamido-dithiolato (N_2S_2) coordination.[14−23] The corresponding mixed amine/amidate complex $(Ni^{II}(HL2))^{-}$ (**3**) also exhibits two ligand field transitions at 22,272 cm^{-1} (340 M^{-1} cm^{-1}) and 17,544 cm^{-1} (a shoulder with $\varepsilon \sim 70$ M^{-1} cm^{-1}) in CH_3OH (Figure 5). The ligand field absorption bands of complex $(Ni^{II}(HL2))^{-}$ (**3**) are shifted slightly to lower energy compared to those of the bisamidate complex $(Ni^{II}(L1))^{2-}$ (**2**). By replacing an amide with an amine in $(Ni^{II}(HL2))^{-}$ (**3**), the anionic charge decreases from −2 to −1, exerting a weaker in-plane ligand field, thereby decreasing the energies of the d → d transitions.

Sulfur K-edge X-ray Absorption Spectroscopy. The sulfur K-edge absorption spectra for $(Ni^{II}(L1))^{2-}$ (**2**) and $(Ni^{II}(HL2))^{-}$ (**3**) are displayed in Figure 6. The pre-edge feature results from the promotion of a S(1s) electron into the unfilled LUMO, which is formally a Ni(3d) orbital. In order for this transition to have any intensity, the orbital must have some degree of S(3p)-character from Ni/S covalency. Therefore, integration of the area under this peak is a direct measure of the Ni/S covalent character of this orbital.

The bisamidate compound $(Ni^{II}(L1))^{2-}$ (**2**) has a normalized peak intensity of 0.57(2) relative to the edge, while that of the mixed amine/amidate compound $(Ni^{II}(HL2))^{-}$ (**3**) has a normalized peak intensity of 0.88(2) relative to the edge. This corresponds to a %S(3p) character of 21(1) and 31(1)% for $(Ni^{II}(L1))^{2-}$ (**2**) and $(Ni^{II}(HL2))^{-}$ (**3**), respectively. These compare well with the previously determined[37] %S(3p) character of the structurally related $(Ni^{II}(BEAAM))^{-}$ (BEEAM = *N*-{2-[benzyl(2-mercapto-2-methylpropyl)amino]ethyl-2-mercapto-2-methylpropionamide) and $(Ni^{II}(emi))^{2-}$ (emi = *N*,*N*′-ethylenebis(2-(mercapto)propionamide)) complexes suggesting that the absence of the gem-dimethyl groups is not having a dramatic influence on the LUMO wave functions. Also similar to $(Ni^{II}(BEAAM))^{-}$ and $(Ni^{II}(emi))^{2-}$, there is a shift in the pre-edge feature of $(Ni^{II}(HL2))^{-}$ (**3**) versus $(Ni^{II}(L1))^{2-}$ (**2**) to higher energy by ~0.3 eV. As one would not expect the core S(1s) orbital to be dramatically influenced by the change in N-donor from an amine to an amidate, this signifies a destabilization of the LUMO in the bisamidate complex versus the mixed amine/amidate complex because of ligand-field effects. Therefore, the Ni($3d_{x^2-y^2}$) LUMO of $(Ni^{II}(L1))^{2-}$ (**2**) is situated ~2400 cm^{-1} higher in energy than that of $(Ni^{II}(HL2))^{-}$ (**3**).

77 K Electronic Absorption Spectroscopy. Both $(Ni^{II}(L1))^{2-}$ (**2**) and $(Ni^{II}(HL2))^{-}$ (**3**) were subjected to low-temperature (77 K) electronic absorption measurements to aid in resolving some of the low energy ligand field transitions from one another (Figure 7). As with the room temperature samples, we see a low-energy transition at

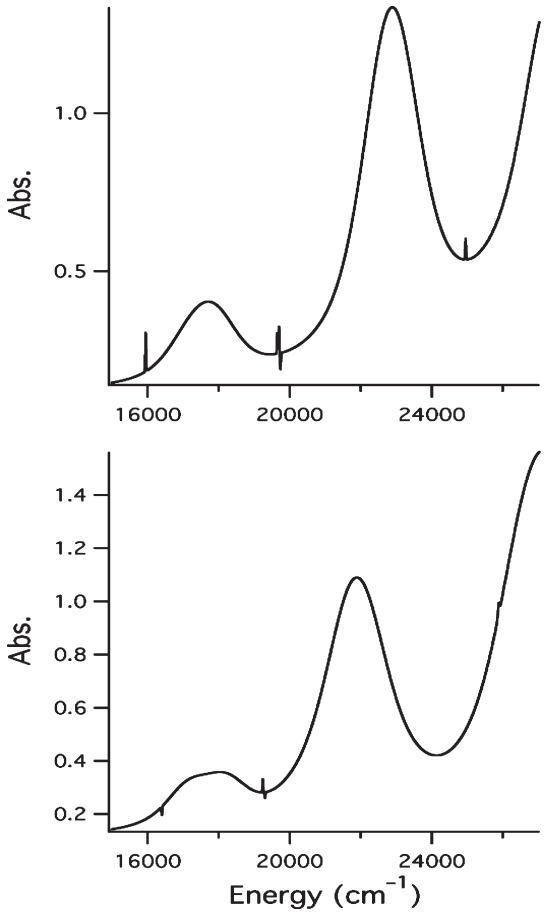

Figure 7. Low temperature (77 K) UV/vis spectra of $(Ni^{II}(L1))^{2-}$ (**2**) (top) and $(Ni^{II}(HL2))^{-}$ (**3**) (bottom).

~22,000 cm^{-1} and a corresponding lower-energy shoulder for both compounds (Supporting Information). For bisamidate ligated $(Ni^{II}(L1))^{2-}$ (**2**), the second derivative of the lower-energy transition shows significant asymmetry. This pronounced asymmetry suggests that this peak is composed of two nearly irresolvable bands at 17,770 and ~17,300 cm^{-1}, which had to be estimated from peak-fitting of the absorption spectrum. In contrast, this band is resolvable into two transitions in the spectrum obtained for amine/amidate ligated $(Ni^{II}(HL2))^{-}$ (**3**), which appear at 17,075 and 18,300 cm^{-1}.

Electrochemistry. The cyclic voltammograms of the mononuclear complexes recorded in DMF solvent are shown in Supporting Information, Figures S4 and S5. A quasireversible Ni^{III}/Ni^{II} redox couple is observed for complex $(Ni^{II}(L1))^{2-}$ (**2**) at −0.129 V versus NHE (−0.849 V vs Fc/Fc^{+}) with a ΔE_p of 123 mV. Conversely, the mixed amine/amidate complex $(Ni^{II}(HL2))^{-}$ (**3**) displays an irreversible oxidation wave at +0.262 V versus NHE (−0.458 V vs Fc/Fc^{+}) and the corresponding reduction wave is not discerned. One possible explanation is that ligand-based oxidation of $(Ni^{II}(HL2))^{-}$ (**3**) results in disulfide formation and is followed by complex decomposition. This is in contrast to the mixed amine/amidate complex reported by Shearer and co-workers[37] which exhibits a quasi-reversible Ni^{III}/Ni^{II} redox couple at approximately 0.320 V versus NHE (−0.330 V vs Fc/Fc^{+}) in CH_3CN.

Oxygenation and Chemical Oxidation Studies. The bisamidate complex $(Ni^{II}(L1))^{2-}$ (**2**) reacts quickly with oxygen in an CH_3CN solution, turning color from red to green within a few minutes. In the UV−visible spectrum, a new peak appears around 350 nm after $(Ni^{II}(L1))^{2-}$ (**2**) was exposed to air. Conversely, the UV−visible spectrum of the mixed amine/amidate complex $(Ni^{II}(HL2))^{-}$ (**3**) exhibited little change even 5 h after being exposed to air in a CH_3OH solution.

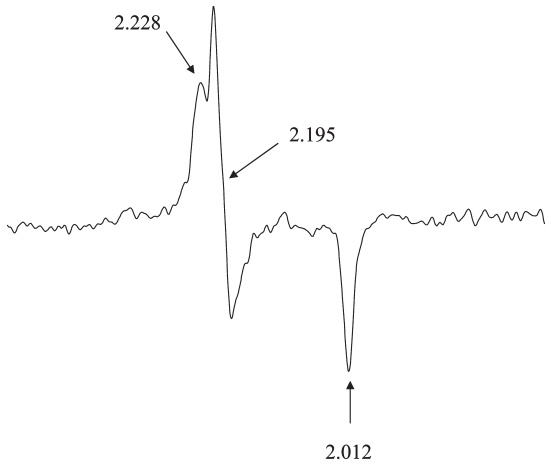

Figure 8. X-band EPR spectrum of the $[Ni^{III}(L1)]^{-}$ in DMF solution made by the chemical oxidation with I_2 at 10 K.

The electrochemical data of complex $(Ni^{II}(L1))^{2-}$ (**2**) suggested the possibility of trapping the Ni^{III} oxidation state. We attempted to generate the Ni^{III} species by chemical oxidation in DMF using I_2. The red bisamidate Ni^{II} complex $(Ni^{II}(L1))^{2-}$ (**2**) turned dark green immediately upon oxidation. The low-temperature EPR spectrum of this oxidized complex (Figure 8) is nearly axial with the experimental g values of $g_1 = 2.012$, $g_2 = 2.195$, and $g_3 = 2.228$ ($g_{av} = 2.145$). These values are indicative of an $S = 1/2$ Ni^{III} species, consistent with those reported previously.[22,23,27d,31] Furthermore, the lack of observable superhyperfine coupling along g_1 is consistent with a four-coordinate Ni^{III} species. Both experimental and computational (see Supporting Information) results suggest the magnitude of the superhyperfine coupling constant would be too small to observed under normal X-band conditions.

Trapping the Ni^{III} species is challenging, presumably because of complex degradation and the formation of EPR-inactive multimeric species, which are also green in color. Thus, it seems that the ability to trap the Ni^{III} complexes depends on various factors and further study is needed to understand more fully the stability of Ni^{III} species. Interestingly, the mixed amine/amidate complex $(Ni^{II}(HL2))^{-}$ (**3**) immediately turned from red to bluish purple upon the addition of I_2, but this complex rapidly decomposed followed by the formation of a precipitate. Attempts to trap oxidized $(Ni^{II}(HL2))^{-}$ (**3**) at low temperatures have been unsuccessful.

Ground-State Electronic Structure of $(Ni^{II}(L1))^{2-}$ (2) and $(Ni^{II}(HL2))^{-}$ (3). DFT geometry optimizations were performed on $(Ni^{II}(L1))^{2-}$ (**2**) and $(Ni^{II}(HL2))^{-}$ (**3**) using the B3LYP hybrid density functional level of theory (TZVP basis set; Supporting Information, Figure S2). Similar to other computational studies on NiN_2S_2 complexes we find that the geometry optimized (GO) structures overestimate the Ni−S and Ni−N bond lengths

Table 3. Selected Computationally-Derived Metric Parameters for $(Ni^{II}(HL2))^{-}$ (**3**), $(Ni^{II}(L1))^{2-}$ (**2**), $Ni^{III}(HL2)$, and $Ni^{III}(BEAAM)$

	(calculated)			
	$(Ni^{II}(HL2))^{-}$ (**3**)	$(Ni^{II}(L1))^{2-}$ (**2**)	Ni^{III} (HL2)	Ni^{III} (BEAAM)
Ni−S(1) (Å)	2.192	2.221	2.153	2.159
Ni−S(2) (Å)	2.215	2.205	2.118	2.147
Ni−N(1) (Å)	1.962	1.884	1.979	1.998
Ni−N(2) (Å)	1.886	1.891	1.860	1.857
Ni−S(1)−N(1) (deg)	172.1	173.2	172.3	168.7
Ni−S(1)−N(2) (deg)	89.6	88.6	89.3	88.6
Ni−S(2)−N(1) (deg)	172.2	172.8	172.1	170.7
Ni−S(2)−N(1) (deg)	92.5	90.0	91.7	91.6
Ni−S(1)−S(2) (deg)	96.7	98.3	94.5	96.5
Ni−N(1)−N(2) (deg)	83.7	84.2	85.1	86.3

relative to the crystal structures. The most significant deviations are found in the Ni-thiolate bond lengths. In the case of the bisamidate $(Ni^{II}(L1))^{2-}$ (**2**), we calculate Ni−S bond lengths of 2.221 and 2.205 Å, while the experimental Ni−S bond lengths are only 2.181 and 2.189 Å. The Ni−N bond lengths, while still overestimated, are more in line with the experimental data (1.884_{calc} vs $1.858_{X\text{-}ray}$ and 1.891_{calc} vs $1.874_{X\text{-}ray}$ Å) (Table 3). Similar trends are observed for the calculated Ni−S bond lengths for $(Ni^{II}(HL2))^{-}$ (**3**) (Table 3). All of the calculated bond lengths are therefore overestimated by no more than 0.045 Å. Previous work has demonstrated that this relatively minor difference in geometries between computationally derived models and the experimental data does not have a large impact on the electronic and energetic properties of the computational versus experimental structures.[65] Thus, the use of more exact computational methods coupled with a larger basis sets is typically not warranted considering the high computational cost, especially for a comparative study.

The LUMOs of $(Ni^{II}(L1))^{2-}$ (**2**) and $(Ni^{II}(HL2))^{-}$ (**3**) are $Ni(3d_{x^2-y^2})/S(\sigma)/N(\sigma)^*$ antibonding in character, while the HOMO and HOMO-1 are both $Ni(3d(\pi))/S(\pi)^*$ in character (Figure 9). Comparison of the degree of S(3p) obtained from the S K-edge studies and the computational results (Löwdin population analysis) shows good agreement between the experimentally and computationally derived values. We observed 31(1)% S(3p)-character in the S K-edge studies for the LUMO of $(Ni^{II}(HL2))^{-}$ (**3**), while the B3LYP calculations for **3** yielded a value of 27.1%. The S K-edge studies demonstrated a reduction in the degree of S(3p)-character for the LUMO of $(Ni^{II}(L1))^{2-}$ (**2**) to 21(1)%, while the B3LYP calculations yielded a value of 19.6% S(3p)-character.[66]

In addition to a decrease in the percentage of S(3p)-character comprising the LUMO of $(Ni^{II}(HL2))^{-}$ (**3**) versus $(Ni^{II}(L1))^{2-}$ (**2**), there is also a decrease in the percentage of S(3p)-character comprising the HOMO and HOMO-1. For $(Ni^{II}(HL2))^{-}$ (**3**), the percentage of S(3p)-character in the HOMO is 68.3% (compared to 32.5% Ni-character), while in $(Ni^{II}(L1))^{2-}$ (**2**), the percentage of S(3p)-character in the HOMO is 52.5% (compared to 36.4% Ni-character) (Figure 9). The trends are similar to those observed for the mixed amine/amidate $Ni^{II}N_2S_2$ compound $(Ni^{II}(BEAAM))^{-}$ and the bisamidate $Ni^{II}N_2S_2$ compound $(Ni^{II}(emi))^{2-}$.[37b] However, the percentage of S(3p)-character in the HOMO of $(Ni^{II}(emi))^{2-}$ and $(Ni^{II}(BEAAM))^{-}$ is approximately 20% lower than found in the corresponding complexes investigated in this study. This is likely responsible for the decreased stability of oxidized $(Ni^{II}(HL2))^{-}$ (**3**) relative to Ni(BEAAM) upon oxidation (vide supra).

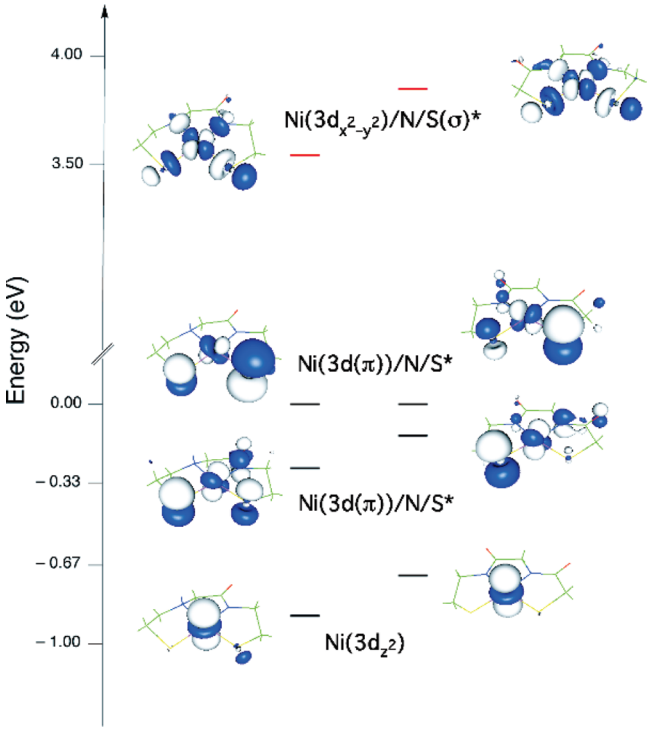

Figure 9. Molecular orbital energy level diagram and iso-surface plot of the LUMO to HOMO-2 of $(Ni^{II}(HL2))^{-}$ (**3**) (left) and $(Ni^{II}(L1))^{2-}$ (**2**) (right). The energies have been normalized to the HOMO, which is the higher-energy $Ni(3d(\pi)/N/S(\pi)^*$ orbital. Doubly filled orbitals are depicted in black while the unfilled LUMO is depicted in red.

The decrease in S(3p)-character in HOMO and HOMO-1 of amine/amidate ligated $(Ni^{II}(HL2))^{-}$ (**3**) versus bisamidate ligated $(Ni^{II}(L1))^{2-}$ (**2**) is a result of two factors. One (minor) factor is the increase in Ni-amide covalency of the bisamidate ligated **2** versus amine/amidate ligated **3**; the HOMO N-amide character increases from 0.2% in $(Ni^{II}(HL2))^{-}$ (**3**) to 2.6% in $(Ni^{II}(L1))^{2-}$ (**2**). The major factor impacting the HOMO and HOMO-1 S(3p)-character is an increase in the overall energy of the 3d-manifold of $(Ni^{II}(L1))^{2-}$ (**2**) relative to $(Ni^{II}(HL2))^{-}$ (**3**). This can be thought of as an increase in the zeroth-order crystal-field strength because of the presence of two anionic amidate donors in **2** versus one anionic amidate and one neutral amine donor in **3**. While this will lead to an overall destabilization of the entire 3d-manifold in $(Ni^{II}(L1))^{2-}$ (**2**), the zeroth-order increase in energy will have a greater influence on the HOMO and HOMO-1. These orbitals are both covalent $Ni(3d(\pi))/S(\pi)^*$ molecular orbitals that result from the overlap of the $Ni(3d_{xz/yz})$ orbitals and the $S(3p_z)$ bonding and anti-bonding combinations (Scheme 2).

(65) Siegbahn, P. E. M. *J. Comput. Chem.* **2001**, *22*, 1634–1645.
(66) For comparison to other Sulfur K-edge X-ray absorption studies, a Mulliken population analysis gives 27.1% S(3p) character in the LUMO for (**3**) and 25.2% for (**2**).

Scheme 2. Simplified Qualitative MO Diagram Depicting the Formation of the HOMO and HOMO-1

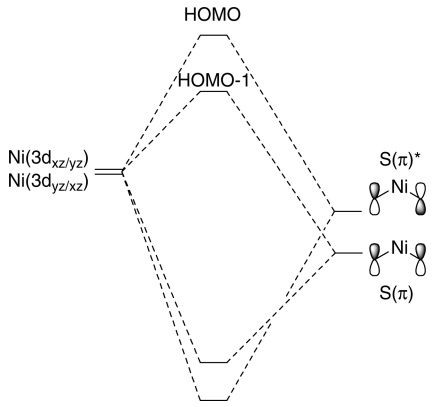

Unlike what is found in amine/amidate ligated **3**, the Ni(3d$_{xz/yz}$) atomic orbitals (AOs) in bis-amidate ligated **2** are higher in energy than the S(π)-fragments. Despite the increased energy of the Ni 3d$_{xz/yz}$ AOs relative to the S(π)-fragments, there is actually a better energy match between the two in $(Ni^{II}(L1))^{2-}$ (**2**) than in $(Ni^{II}(HL2))^{-}$ (**3**). The consequence of this is 3-fold. First, there is a better balance of Ni- and S(3p)-character in the HOMO and HOMO-1 of the bisamidate complex **2** relative to the mixed amine/amidate complex **3** because of better Ni/ligand orbital mixing (i.e., there is higher Ni−S covalency in $(Ni^{II}(L1))^{2-}$ (**2**)). Second, the HOMO of $(Ni^{II}(L1))^{2-}$ (**2**) will have less S(3p)-character and more Ni-character relative to $(Ni^{II}(HL2))^{-}$ (**3**) owing to the increased Ni−S covalency. Third, and most importantly, the HOMO of the bisamidate complex **2** will be energetically activated relative to the mixed amine/amidate complex **3** because of higher Ni−S(3p) covalency. Because the nucleophilic HOMO of $(Ni^{II}(L1))^{2-}$ (**2**) is activated relative to $(Ni^{II}(HL2))^{-}$ (**3**), it should be significantly more reactive toward electrophilic O_2, which is what is observed experimentally.

Excited-State Calculations of $(Ni^{II}(L1))^{2-}$ (2) and $(Ni^{II}(HL2))^{-}$ (3). To determine the origin of the features in the electronic absorption spectra of $(Ni^{II}(L1))^{2-}$ (**2**) and $(Ni^{II}(HL2))^{-}$ (**3**), we performed excited-state electronic structure calculations on the two transition metal compounds. Excited-state calculations were carried out using Neese's SORCI methodology, which has yielded excellent results in calculating the electronic absorption spectra of transition metal complexes in cases where methods such as time dependent DFT (TD-DFT) have failed. A complete discussion of the excited-state calculations and their results can be found in the Supporting Information. For both complexes the four lowest energy transitions can be thought of as arising from within the 3d manifold (i.e., are d → d transitions) and their leading configurations are attributed to: 3d$_{xz/yz}$ → 3d$_{x^2-y^2}$, the 3d$_{yz/xz}$ → 3d$_{x^2-y^2}$, 3d$_{z^2}$ → 3d$_{x^2-y^2}$, and the 3d$_{xy}$ → 3d$_{x^2-y^2}$ transitions. Because the "3d$_{z^2}$ MO" is mostly AO in character (98.2% 3d$_{z^2}$ in character), the intensity of the 3d$_{z^2}$ → 3d$_{x^2-y^2}$ is low, and one would not expect that it could be readily resolved from the experimental data, which is what is observed experimentally (vide infra). In contrast, we find that the other ligand-field transitions arise from final state wave functions that have (a) significant multiconfigurational character, and (b) significant ligand character. The large multiconfigurational character of the final state wave functions explains why TD-DFT, which is a single-determinantal method, cannot adequately reproduce the electronic absorption spectra for these complexes.

Upon the addition of the second amidate ligand, the energy of the ligand-field transitions all increase in energy. The lowest energy transition, the "3d$_{xz/yz}$ → 3d$_{x^2-y^2}$" transition, occurs ~1450 cm^{-1} higher in energy in bis-amidate ligated **2** than in amine/amidate ligated **3**. The next highest energy transition, the "3d$_{yz/xz}$ → 3d$_{x^2-y^2}$" transition, is also higher in energy in $(Ni^{II}(L1))^{2-}$ (**2**) than $(Ni^{II}(HL2))^{-}$ (**3**). However, because of the increased amide character in the excited-state wave function of this transition in the amine/amidate ligated **3**, the 3d$_{yz/xz}$ → 3d$_{x^2-y^2}$ transition occurs only 600 cm^{-1} higher in energy in $(Ni^{II}(L1))^{2-}$ (**2**) versus $(Ni^{II}(HL2))^{-}$ (**3**). Therefore, the splitting in energy of the 3d$_{xz/yz}$ → 3d$_{x^2-y^2}$ versus 3d$_{yz/xz}$ → 3d$_{x^2-y^2}$ transition in $(Ni^{II}(L1))^{2-}$ (**2**) is calculated to be much smaller in magnitude than in $(Ni^{II}(HL2))^{-}$ (**3**) (~780 vs 1600 cm^{-1}). In both cases the most prominent ligand-field transition at ~22,000 cm^{-1} is predicted to be the "3d$_{xy}$ → 3d$_{x^2-y^2}$" transition.[32a,34,37] Because of the higher degree of ligand character in this transition for $(Ni^{II}(L1))^{2-}$ (**2**) versus $(Ni^{II}(HL2))^{-}$ (**3**) from mixing of lower-energy ligand centered states, this transition is more charge-transfer like in $(Ni^{II}(L1))^{2-}$ (**2**) than in $(Ni^{II}(HL2))^{-}$ (**3**). Thus, it has larger calculated oscillator strength in $(Ni^{II}(L1))^{2-}$ (**2**) than in $(Ni^{II}(HL2))^{-}$ (**3**) (0.0077 vs 0.0055).

Energy Level Description of $(Ni^{II}(L1))^{2-}$ (2) vs $(Ni^{II}(HL2))^{-}$ (3). Using the S K-edge data, electronic absorption measurements, and excited-state computational results we can create an accurate picture of the valence orbitals in $(Ni^{II}(L1))^{2-}$ (**2**) and $(Ni^{II}(HL2))^{-}$ (**3**) (Scheme 3). Descending from the totally symmetric free ion into D_{4h} symmetry, the lowest energy transitions correspond to the $^1E_g \leftarrow {}^1A_{1g}$, $^1B_{2g} \leftarrow {}^1A_{1g}$, and $^1A_{2g} \leftarrow {}^1A_{1g}$ transitions (see Scheme 3 for orbital descriptions of these states). These all further descend into $^1A \leftarrow {}^1A$ transitions because of the asymmetry of the ligand environment. In $(Ni^{II}(L1))^{2-}$ (**2**) and $(Ni^{II}(HL2))^{-}$ (**3**), the weak $^1A(B_{2g}) \leftarrow {}^1A$ transition is obscured by the other ligand field transitions, while the $^1E_g \leftarrow {}^1A_{1g}$ transition is split into two $^1A(E_g) \leftarrow {}^1A$ transitions as a result of the lower symmetry presented by the ligand field environment. As expected, the splitting of the ^1E_g state is larger for amine/amidate ligated $(Ni^{II}(HL2))^{-}$ (**3**) than it is for bisamidate ligated $(Ni^{II}(L1))^{2-}$ (**2**); there is approximately a 1,225 cm^{-1} splitting of the ^1E_g state in $(Ni^{II}(HL2))^{-}$ (**3**) compared to a less than 470 cm^{-1} splitting of the ^1E_g state in $(Ni^{II}(L1))^{2-}$ (**2**).

The S K-edge X-ray absorption spectra indicate that the Ni(3d$_{x^2-y^2}$) LUMO of bisamidate ligated $(Ni^{II}(L1))^{2-}$ (**2**) is approximately 2400 cm^{-1} higher in energy than that of $(Ni^{II}(HL2))^{-}$ (**3**). Using the energies obtained from the low-temperature (77 K) electronic absorption spectra, we can arrive at reasonable estimates of the relative energies of the HOMO for both of these complexes. The corresponding difference of the lowest energy $^1A(E_g) \leftarrow {}^1A$ for bisamidate ligated $(Ni^{II}(L1))^{2-}$ (**2**) versus amine/amidate ligated $(Ni^{II}(HL2))^{-}$ (**3**) is approximately 225 cm^{-1}. Considering that a ligand-field analysis suggests that the Slater−Condon−Shortley parameters for the two

Scheme 3. Energy Level Correlation Diagram for the Square-Planar Low-Spin Ni^{II} Ion

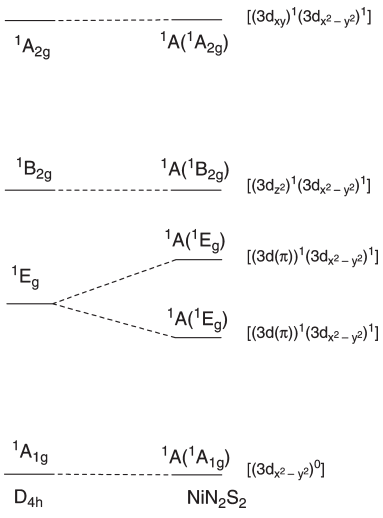

complexes are approximately the same (a 78 vs 76% reduction from the atomic values for **2** vs **3**), we can assume a similar degree of e^-/e^- repulsion within the d-orbitals. Thus, when this difference in energy is subtracted from the energy difference of the LUMO, we surmise that the HOMO in bisamidate ligated $(Ni^{II}(L1))^{2-}$ (**2**) is activated by ~2175 cm^{-1} (~6.2 kcal mol^{-1}) relative to amine/amidate ligated $(Ni^{II}(HL2))^-$ (**3**).[67] *The activation of the HOMO in the bisamidate ligated* $(Ni^{II}(L1))^{2-}$ (**2**) *is largely responsible for its increased* O_2 *sensitivity relative to amine-amidate ligated* $(Ni^{II}(HL2))^-$ (**3**). The nucleophilic doubly filled Ni(3dπ)/S(π)* HOMO is electronically tuned to be more reactive toward electrophiles like O_2 relative to that of $(Ni^{II}(HL2))^-$ (3).

Electronic Structure of Ni^{III}(BEAAM) and Ni^{III}(HL2). To gain better insight into the irreversibility observed in the CV of $(Ni^{II}(HL2))^-$, we performed electronic structure calculations on oxidized Ni^{III}(HL2) at the B3LYP level of theory to compare with those performed on Ni^{III}(BEAAM). GO structures (Supporting Information, Figure S3) for both Ni^{III}(HL2) and Ni^{III}(BEAAM) are nearly identical to one another, which is expected considering that both are $Ni^{III}N_2S_2$ complexes with mixed amine/amidate ligation with 5,5,5-chelate rings (Table 3). Predictably, the Ni-ligand bond lengths are all contracted relative to the reduced Ni^{II} GO structures. Ni^{III}(HL2) has calculated Ni−S bond lengths of 2.153 (trans amine) and 2.118 Å (trans amide), while the calculated Ni−N bond lengths are 1.979 (amine) and 1.860 Å. Similarly, Ni^{III}(BEAAM) possesses calculated Ni−S bond lengths of 2.159 (trans amine) and 2.147 Å (trans amide) and calculated Ni−N bond lengths of 1.998 (amine) and 1.857 Å. The elongation of the Ni−S bond trans to the amide nitrogen in Ni^{III}(BEAAM) relative to Ni^{III}(HL2) is due to steric crowding; the gem-dimethyl groups of Ni^{III}(BEAAM) are in close contact with both the amine substituent and the hydrogens of the ethylene backbone forcing the Ni−S bond to elongate to relieve steric repulsion.

Single point hybrid-DFT calculations of these Ni^{III} compounds point toward the reason for the reduced stability upon oxidation on the CV time scale for $(Ni^{II}(HL2))^-$ (**3**) compared to $(Ni^{II}(BEAAM))$, which displays a quasi-reversible Ni^{III}/Ni^{II} couple.[37] A Löwdin population analysis shows that the singly occupied molecular orbital (SOMO)[68] of Ni^{III}(HL2) is composed of 71.4% S(3p)-character and only 8.3% Ni-character. This can be contrasted with Ni^{III}(BEAAM), which has a SOMO that is composed of 59.7% S(3p)-character and 26.6% Ni-character, indicating that less electron density resides on the metal in Ni^{III}(HL2) relative to Ni^{III}(BEAAM). This would lead to a less stable oxidized species in Ni^{III}(HL2) compared to Ni^{III}(BEAAM), as it would contain more S· character. As sulfur-centered radicals are highly reactive species, the increased S· character in the SOMO of Ni^{III}(HL2) versus Ni^{III}(BEAAM) would lead to a much more chemically reactive species, and thus irreversibility in the CV of Ni^{III}(HL2).

Discussion

The active site of reduced Ni-SOD and the Ni_d-site of ACS both contain a Ni ion ligated in an N_2S_2 coordination environment, and yet the properties of the two Ni^{II} ions are very different. In Ni-ACS, the NiN_2S_2 site does not seem to be involved in the catalytic redox cycle,[2,6b] while in Ni-SOD the Ni ion switches between the Ni^{II} and Ni^{III} state during the catalytic cycle.[26,69] Interestingly, the Ni-SOD active site utilizes a mixed amine/amidate ligation as opposed to the bisamidate ligation found in the Ni_d(Cys-Gly-Cys) site of ACS. Thus, a small difference in coordination environment around nickel apparently leads to very different properties of the NiN_2S_2 site in these two enzymes. It is possible that the sulfurs in Ni-SOD are protected by second coordination sphere effects, hydrogen bonding, and/or steric interactions rather than inner sphere coordination effects. However, all bisamidate $Ni^{II}N_2S_2$ complexes reported to date are exceedingly air-sensitive, while the active site of Ni-SOD is apparently stable to O_2, superoxide, and hydrogen peroxide, providing further evidence that slight differences in coordination environment can have a profound impact on the properties of the Ni^{II} ions. Our results can be added to a small but growing body of evidence indicating that electronic tuning of the Ni-SOD active site is at least partially responsible for the increase the stability of the Ni-SOD active site toward reactive oxygen species.[27b,29,34,37]

To understand more fully the reason for this difference in reactivity, we synthesized and characterized a set of model complexes with NiN_2S_2 coordination that differ only in amidate versus amine ligation. These complexes correlate well with the reduced active site of Ni-SOD and distal nickel site of ACS and are therefore able to provide unique insight into how the enzymes tune the Ni center to achieve very different properties for the similar NiN_2S_2 site.

(67) If the differences in e^-/e^- repulsion are considered then the HOMO activation of $(Ni^{II}(L1))^{2-}$ (**2**) vs $Ni^{II}(HL2)^-$ (**3**) could be as high as ~3000 cm^{-1}. However, we consider the 78 vs 76% reduction in the Slater−Condon−Shortley parameters to be within the error of the data fitting.

(68) We refer to the highest filled spin-up MO as the SOMO, which is largely 3d(π)-S(π) in character.

(69) Bryngelson, P. A.; Maroney, M. J. In *Nickel and Its Surprising Impact in Nature*; Sigel, A., Sigel, H., Sigel, R. K. O., Eds.; John Wiley & Sons: Chichester, U.K., 2007; Metal ions in Life Sciences, Vol. *2*; Chapter 9, pp 417−444.

The X-ray structures of the mononuclear complexes $(Ni^{II}(L1))^{2-}$ (**2**) and $(Ni^{II}(HL2))^{-}$ (**3**) show that the Ni^{II} ions are in a square-planar coordination geometry. In complex $(Ni^{II}(L1))^{2-}$ (**2**), the asymmetrically positioned carbonyl groups in the ligand backbone impose slight differences in the bond lengths and angles compared to the analogous 5,5,5 chelated NiN_2S_2 planar complexes.[14,22b] In the mixed amine/amidate complex $(Ni^{II}(HL2))^{-}$ (**3**), the Ni−N(amide) bond distance is shorter than the Ni−N(amine) bond distance while the Ni−S (trans to the amide nitrogen) bond distance is longer than the Ni−S(trans to amine nitrogen). This is as expected because the N(amide) ligands are stronger σ-donors than N(amine) ligands, and thus exhibit a larger trans influence. In comparison to the mixed amine/amidate complex Ni(BEAAM) reported by Shearer and co-workers,[37] the difference in the bond lengths of the Ni−S bonds trans to the N(amide) versus N(amine) is smaller in $(Ni^{II}(HL2))^{-}$ (**3**). This difference may be due to steric crowding from the gem-dimethyl groups in Ni(BEAAM) and/or the presence of the secondary amine nitrogen in $(Ni^{II}(HL2))^{-}$ (**3**) as opposed to a tertiary amine nitrogen.

A comparison of the optical spectra of the bisamidate complex $(Ni^{II}(L1))^{2-}$ (**2**) and the mixed amine/amidate complex $(Ni^{II}(HL2))^{-}$ (**3**) reveals that absorption bands for the latter are at slightly lower energy. This can be easily rationalized from a simple crystal-field point of view. The additional anionic amidate in $(Ni^{II}(L1))^{2-}$ (**2**) versus $(Ni^{II}(HL2))^{-}$ (**3**) in the equatorial plane leads to a significant destabilization of the $Ni(3d_{x^2-y^2})$ orbital, which in turn increases the energy of the ligand-field transitions in the bisamidate complex. This simplistic view is fully supported by our electronic structure calculations. Although the energy of the Ni 3d(π)-type HOMO and HOMO-1 of $(Ni^{II}(L1))^{2-}$ (**2**) are significantly destabilized relative to those of $(Ni^{II}(HL2))^{-}$ (**3**), the LUMO rises even higher in energy in $(Ni^{II}(L1))^{2-}$ (**2**) because of the stronger σ-bonding interaction between the two amide-nitrogens and the $Ni(3d_{x^2-y^2})$, resulting in a higher energy transition.

The influence of amine versus amide bonding is also reflected in the electrochemical properties of the complexes. As expected, the bisamidate complex $(Ni^{II}(L1))^{2-}$ (**2**), displays a more negative Ni^{III}/Ni^{II} oxidation potential than the mixed amine/amidate complex $(Ni^{II}(HL2))^{-}$ (**3**). This can be easily explained by the fact that the electron-rich bisamidate ligand better stabilizes the Ni^{III} oxidation state. This is supported by DFT calculations which indicate that the redox active molecular orbital (RAMO) is destabilized in the bisamidate complex.

The DFT calculations also provide insight into the stability of the Ni^{III} complexes. Experimentally we observe that the bisamidate complex $(Ni^{II}(L1))^{2-}$ (**2**) is more stable with respect to one-electron oxidation relative to mixed amine/amidate complex $(Ni^{II}(HL2))^{-}$. This can be explained by the fact that the RAMO in $(Ni^{II}(L1))^{2-}$ (**2**) has less S(3p)-character. Thus, the resulting radical will contain more Ni character and less S character. Interestingly, the oxidation of the complex $(Ni^{II}(HL2))^{-}$ (**3**) is completely irreversible while the one-electron oxidation of a similar mixed amine/amidate complex, Ni(BEAAM), reported by Shearer and co-workers[37] is quasi-reversible. From the single-point DFT calculations, a Löwdin population analysis reveals that the SOMO[68] of $Ni^{III}(HL2)$ is composed of 71.4% S(3p)-character and only 8.3% Ni-character. This can be contrasted with Ni^{III}(BEAAM), which has a SOMO that is composed of 59.7% S(3p)-character and 26.6% Ni-character. This implies that $Ni^{III}(HL2)$ has a significant increase in S(3p)-character relative to Ni^{III}(BEAAM). Thus, upon oxidation there will be more sulfur-based radical character in oxidized $Ni^{III}(HL2)$ than in Ni^{III}(BEAAM), which should make $Ni^{III}(HL2)$ significantly more unstable than Ni^{III}-(BEAAM). Also, the increased steric bulk of the gem-dimethyls of Ni^{III}(BEAAM) α to the thiolate ligands will lead to additional stability of the oxidized complex relative to $Ni^{III}(HL2)$. This is manifested in the irreversibility of $Ni^{III}(HL2)$ on the CV time scale. We note, however, that the Ni^{III} forms have not been successfully isolated for either complex, suggesting that the reduced amount of sulfur based radical character in Ni^{III}(BEAAM) versus $Ni^{III}(HL2)$ is still not sufficient to stabilize adequately the complex on longer time-scales.

The electrochemical data of the complex $(Ni^{II}(L1))^{2-}$ (**2**), suggest that the Ni^{III} formed by chemical oxidation should be detectable by EPR. The EPR spectrum of the chemical oxidation product of $(Ni^{II}(L1))^{2-}$ (**2**) in DMF (Figure 8) displays a nearly axial EPR signal with g values of $g_1 = 2.012$, $g_2 = 2.195$, and $g_3 = 2.228$ ($g_{av} = 2.145$), indicative of a Ni^{III} formulation with $S = 1/2$ and with the unpaired electron residing in a $Ni(d_{z^2})$ orbital. This spectrum is consistent with the Ni^{III} EPR spectra reported by Holm,[22] Krüger,[22,23] and Brunold,[31] and with our DFT calculations at the B3LYP level (Supporting Information). In the case of complex $(Ni^{II}(HL2))^{-}$ (**3**), the chemical oxidation with I_2 forms a purple species which is not stable and decays within seconds. Attempts to trap the Ni^{III} species even at low temperature have not been successful, consistent with the electrochemical irreversible behavior. Again from the DFT calculations, a Löwdin population analysis shows that the SOMO of Ni^{III}-(HL2) is composed of 71.4% S(3p)-character and only 8.3% Ni-character. This implies $Ni^{III}(HL2)$ has a significant increase in highly reactive radical S(3p)-character and may preclude its isolation because of sample decomposition.

The bisamidate complex $(Ni^{II}(L1))^{2-}$ (**2**) is highly reactive toward O_2 in CH_3CN, while the mixed amine/amidate complex $(Ni^{II}(HL2))^{-}$ (**3**) is considerably less reactive and is stable for at least a week in solution. This agrees with our predictions from the DFT studies that the bisamidate compound $(Ni^{II}(L1))^{2-}$ (**2**) should be more O_2 sensitive than $(Ni^{II}(HL2))^{-}$ (**3**). This is because the filled Ni(3d(π))/S(π)* HOMO in $(Ni^{II}(L1))^{2-}$ (**2**) acts as a nucleophile toward the electrophilic O_2 molecule.[27b,28,29,37] Increasing the energy of the HOMO via an increase in Ni−S covalency in $(Ni^{II}(L1))^{2-}$ (**2**) effectively activates this species toward electrophiles relative to $(Ni^{II}(HL2))^{-}$ (**3**). These results are consistent with previously reported Ni-SOD model compounds containing mixed amine/amidate $Ni^{II}N_2S_2$ coordination that are also air-stable.[37,38]

Similar reasoning also explains the formation of the trinuclear complex $(\{Ni^{II}(L1)\}_2Ni^{II})^{2-}$ (**1**) and the fact that $(Ni^{II}(HL2))^{-}$ (**3**) remains mononuclear in solution. The thiolates of $(Ni^{II}(L1))^{2-}$ (**2**) are far more nucleophilic than observed in $(Ni^{II}$-$(HL2))^{-}$ (**3**). Thus, $(Ni^{II}(L1))^{2-}$ (**2**) rapidly forms a stable trinuclear complex in solution with any "free" Ni ions. In contrast, $(Ni^{II}(HL2))^{-}$ (**3**) reacts sluggishly with Ni ions, precluding the formation of the corresponding trinuclear species.

In summary, we synthesized and characterized two new NiN_2S_2 complexes which serve as models for the Ni_d site of

ACS and the active site of reduced Ni-SOD to advance our understanding of how the amine versus amide coordination environment influences the properties of the Ni ion. The complex $(Ni^{II}(HL2))^{-}$ (**3**) is one of the few examples of a synthetic mixed amine/amidate Ni^{II} species reported. Our results demonstrate that the bisamidate complex $(Ni^{II}(L1))^{2-}$ (**2**) is considerably more reactive toward O_2 and susceptible to trimer formation than the corresponding mixed amine/amidate complex $(Ni^{II}(HL2))^{-}$ (**3**). SORCI calculations in combination with S K-edge X-ray absorption spectroscopy and low-temperature electronic absorption measurements reveal that the additional amidate ligand in $(Ni^{II}(L1))^{2-}$ (**2**) destabilizes the HOMO by ~6.2 kcal mol^{-1} relative to $(Ni^{II}(HL2))^{-}$ (**3**). The consequence of this destabilization is manifested in the nucleophilic activation of the doubly filled HOMO, which makes $(Ni^{II}(L1))^{2-}$ (**2**) significantly more reactive toward electrophiles. This explains why Ni-SOD utilizes the NiN_2S_2 mixed amine/amidate coordination environment; this coordination environment deactivates the nucleophilic S(π)-type HOMO toward attack (as demonstrated by our model complexes) thereby allowing Ni-SOD to perform Ni-centered oxidation and avoid thiolate oxygenation.

Acknowledgment. We acknowledge financial support from the National Science Foundation (CHE-0348777). We thank Dr. Atta Arif (University of Utah) for solving the X-ray structure of **3** and Thomas Casey (Michigan State University) for EPR measurements. Computational resources provided by the Research Computing Grid at the University of Nevada, Reno. J.S. thanks the NIH (P20 RR-016464) and the NSF (CHE-0844234) for support.

Supporting Information Available: Excited-state calculations of $(Ni^{II}(L1))^{2-}$ (**2**) and $(Ni^{II}(HL2))^{-}$ (**3**), computationally derived structures, Mulliken population analysis, Löwdin population analysis, results from the SORCI calculations, computationally derived coordinates, calculated EPR parameters, electronic absorption data from the low-temperature solid-state samples, cyclic voltammograms, and X-ray structural data in CIF format. This material is available free of charge via the Internet at http://pubs.acs.org.